Dynamics of phase separation of sheared binary mixtures after a nonisothermal quenching

Antonio Bertei [1,*,†] Chih-Che Chueh [2,†] and Roberto Mauri [1]
[1] *Department of Civil and Industrial Engineering, University of Pisa, Largo Lucio Lazzarino 2, 56122 Pisa, Italy*
[2] *Department of Aeronautics and Astronautics, National Cheng Kung University, Tainan 701, Taiwan*

(Received 9 November 2020; accepted 20 August 2021; published 8 September 2021)

When a symmetric regular binary mixture, subjected to a constant shear, is quenched into the unsteady region of its phase diagram under a temperature gradient, it phase separates following very complicated patterns. The phase separation process is simulated using a thermodynamics-based phase-field model where the fundamental balance equations are coupled with the constitutive equations for the diffusive fluxes of chemical species, momentum, and energy by applying the rules of nonequilibrium thermodynamics. The evolution of phase separation shows distinct features, being more complex than a simple superposition of patterns emerging in a shear flow and under a thermal gradient when taken individually. The imposed temperature gradient causes a preferential nucleation at the cooler wall, so that the emerging droplets drift towards the center of the domain while following the imposed flow field, causing a change in droplet movement as they cross the domain centerline and enhancing coalescence. The imposed temperature gradient breaks the symmetry compared to instantaneous quenching, with stable droplets which remain attached to the cooler wall and move coherently with it. The capillary number (N_{Ca}) determines breakup and phase separation evolving as stripes for $N_{\mathrm{Ca}} \gg 1$, while droplets nucleate and grow for $N_{\mathrm{Ca}} \ll 1$. The Lewis number (N_{Le}) affects the pace and propagation of phase separation: for $N_{\mathrm{Le}} > 10$ phase separation takes place rather uniformly, being similar to instantaneous quenching, while for $N_{\mathrm{Le}} < 0.1$ the mixture cools slowly and a phase separation front proceeds from the cooler wall. A similar behavior is induced by a composition-dependent thermal conductivity. The mixture dimensionless heat capacity (N_c) has a significant effect on phase separation because, for $N_c \ll 1$, heat dissipation counterbalances the effect of the applied temperature quench, thus retarding or even reversing the process of phase separation. These results and the variety of patterns reproduced by the model highlight the necessity of integrating a consistent thermodynamic description to the hydrodynamics and heat transport in phase-field modeling.

DOI: 10.1103/PhysRevFluids.6.094302

I. INTRODUCTION

A mixture of two (or more) liquids is considered to be partially miscible when it exhibits a miscibility gap, i.e., there is a range of compositions where, at equilibrium, it forms a two-phase liquid system. In most cases, miscibility increases with temperature, so that there is an upper critical temperature, above which the liquids are miscible in all compositions. Following a temperature drop from the single-phase region of the phase diagram to its unstable part, the initially homogeneous

*antonio.bertei@unipi.it
†These authors contributed equally to this work.

mixture becomes unstable to arbitrarily small fluctuations and therefore it phase separates [1]. In the absence of any externally imposed flow field, this process consists of the formation of small nuclei that coalesce and grow, following a universal scaling $L(t) \propto t^{\beta}$ of the domain mean size with time [2,3]. For extremely viscous systems, like melted alloys, or for millikelvin temperature quenches, diffusion is the dominant transport mechanism; in these cases, it is well known, both experimentally [4,5] and theoretically [6], that the critical exponent is $\beta = 1/3$. In general, this exponent law is the signature of coalescence driven by Brownian motion [7]. On the other hand, for larger temperature quenches or in liquid mixtures, coalescence is driven by hydrodynamic, long-range interactions, as convection dominates diffusion; in this case, it was shown dimensionally [3,8] that the growth law $L(t) \approx (\sigma/\eta)t$ is obtained for small Reynolds number (while for large Reynolds numbers, a $2/3$ power law is obtained), with η and σ denoting viscosity and surface tension, respectively, thus confirming experimental results [9–12].

As for the theoretical modeling, processes such as coalescence and breakup of bubbles and drops occur at a length scale of the order of the interface thickness, and therefore they can hardly be described by using the classical two-phase flow approach, where the different phases are assumed as being at thermodynamic equilibrium, separated from each other by a sharp interface, i.e., a zero-thickness region of space [13]. The fundamental drawback of the free-boundary approach is resolved by the phase-field, or diffuse interface, model, dating back to a seminal work by van der Waals [14], based on the assumption that all physical quantities are described by continuous functions, i.e., they are "diffuse." When the system is separated in two coexisting phases, even the quantities, such as density and concentration, that in the free-boundary approach change discontinuously at the interface, here change gradually within an interfacial volume, with a steep gradient in a direction normal to the interface. Therefore, the phase-field approach assumes that the order parameters change within a characteristic interface thickness, a, so that in the limit of vanishing a, the classical free-boundary approach is recovered [15–17].

Conceptually, the starting point of the phase-field approach is that we can describe the system via an energy functional which can be expanded in terms of gradients of the order parameter (see review in Lamorgese *et al.* [18]), thus including nonlocal effects. Consequently, adopting the phase-field approach means that all the balance equations must be modified, to include new nonlocal terms in the constitutive equations of the fluxes of chemical species, momentum, and energy.

In the 1930s, van der Waals theory was generalized by Ginzburg and Landau to model all order-disorder phase transition processes and thereby describing phenomena such as ferromagnetism, superfluidity, and superconductivity [19]. The phase-field model was applied by Cahn and Hilliard [20,21] to perform a linear stability analysis of the diffusion-driven spinodal decomposition of alloys, following an instantaneous temperature quench. As this process is supposed to be isothermal and convection free, it is governed by a single diffusion equation for the concentration field, that was subsequently resolved numerically (see Vladimirova *et al.* [22] and references therein), leading to results in agreement with the $L \propto t^{1/3}$ scaling predicted theoretically and measured experimentally.

Modeling convection proved to be more complicated. First, in 1901, Korteweg [23] proposed an expression for the capillary stresses, which are generally referred to as Korteweg stresses. Within the interfacial region, these stresses determine a body force, reducing to surface tension when the interfacial region collapses into a sharp interface; on the other hand, the Korteweg body force vanishes identically within a single-phase region at equilibrium. In low viscosity liquids and/or following deep quenches (i.e., in conditions far from thermodynamic equilibrium), the Korteweg force induces a strong convective motion, which enhances coalescence among drops and accelerates heat transfer. When the resulting momentum equation is coupled with the convection-diffusion equation for the composition field, we obtain the Cahn-Hilliard-Stokes-Korteweg (CHSK) equations, otherwise called model H in Hohenberg and Halperin's taxonomy [24]. Applying this model, the convection-driven phase separation of viscous binary mixtures was simulated numerically (see Vladimirova *et al.* [25] and Lamorgese *et al.* [26], and references therein), leading to results that agree with the $L \propto t$ and $L \propto t^{2/3}$ scaling predicted

theoretically and measured experimentally. In addition, the model was also applied to simulate the deformation [27], breakup [28,29], and coalescence [30] of thermodynamically stable droplets.

In comparison with the effort devoted into finding efficient numerical schemes to solve the CHSK equations, little attention was paid into adding an energy balance equation and to study the case of nonisothermal fluid mixtures. In fact, most of the published works on the modeling and numerical simulations of liquid-liquid phase separation assume an instantaneous quench to a final (uniform) temperature within the unstable or metastable regions of the phase diagram, whereby an isothermal separation process is assumed. Some attempts to simulate the heat transfer rates during spinodal decomposition of a critical solution were reported [31]; however, the energy source term due to internal frictions and phase separation was typically neglected [31,32]. Furthermore, the temperature variation of a, i.e., the length scale representing the spatial inhomogeneity of the separating phases, has not been appropriately modeled. This overlook, which might undermine the reliability of the modeling works, can be arguably explained as follows: while a CHSK scheme could be devised for a very simple model system, although having little resemblance to real mixtures, the energy equation requires a proper thermodynamic setting. Excellent results were obtained for the phase separation of van der Waals fluids [33,34]. However, in general, when proper thermodynamically consistent models were proposed [35–39], the number of independent parameters was too large to obtain easily understandable results. Then, Molin and Mauri [40] proposed a phase-field model for regular binary mixtures, combining thermodynamic consistence with the simplicity of the model. In this work it was shown that heat transfer can be enhanced by phase separation, in agreement with experimental findings [41]. This model was subsequently generalized and applied to different problems (see reviews in Lamorgese *et al.* [26] as well as Lamorgese *et al.* [18] and Segal [42]), always with simplifying assumptions that will be removed in the present work.

Here, phase separation of a regular binary mixture following a nonuniform temperature quench and under shear flow is considered. Previous studies have shown how the dynamics of phase separation evolves in a shear flow during an instantaneous quench, featuring droplet morphologies ranging from elongated bands to round shapes [43], or in a quiescent fluid under a temperature gradient, where a dynamic transition in the orientation of nuclei was observed [44]. Considering the strong coupling between hydrodynamics, heat transport, and mixture thermodynamics, the combination of shear flow and temperature gradient can give rise to specific features of system evolution during phase separation, going beyond the simple superposition of the individual behaviors. Therefore, the phase separation of sheared mixtures upon a temperature gradient is considered here as an example to showcase how a thermodynamics-based phase-field model can capture the complex interplay between hydrodynamics, mixture thermodynamics, and heat transport, thus further shedding light on the underlying transport phenomena.

After a summary of the governing equations, whose detailed derivation is reported in the Appendixes, the model is applied to investigate how the dynamics of phase separation is affected by different fluid and thermal properties such as heat capacity, thermal conductivity, the ratio between mass and heat diffusion, as well as the capillary number. While simpler behaviors in case of no shear [32,44] or instantaneous quenching [43] are readily recovered, thus providing validation of the numerical scheme, the set of numerical simulations here presented highlights the variety of extremely different morphologies of phase separation evolution under temperature and velocity gradients by varying the properties of the fluid. Finally, a few concluding remarks are presented in the last section.

II. MODELING

The governing equations describe the evolution of the composition, momentum, and energy fields of a binary mixture of two species, *1* and *2*, using a thermodynamics-based diffuse interface approach developed by Mauri and co-workers [18,26], which consistently links transport and capillary phenomena to mixture thermodynamics. As the problem is complex, a few simplifying assumptions are introduced to reduce model complexity to the relevant elementary phenomena [43]:

(i) species *1* and *2* have the same molecular weight, $M_1 = M_2 = M_w$; (ii) mass density ρ is constant and independent of temperature and composition; thus, the mixture is treated as incompressible; and (iii) the mixture is regular and symmetric, representing a van der Waals fluid, so that the excess free energy is described in terms of a single Margules parameter Ψ (also denoted as the van Laar or Flory-Huggins interaction parameter). In this section, first we describe the governing equations and the mixture thermodynamics, then the problem is formulated in dimensionless form, showing how the relevant dimensionless quantities are defined. A detailed derivation of the framework is reported in the Appendixes while only the final equations strictly relevant for the simulations are reported in the following.

A. Equations of motion

For a binary mixture, in the absence of chemical reactions and under the assumptions listed above, the governing equations are the conservation of mass, momentum, chemical species, and energy, which read as follows [see Eqs. (B11)–(B14) in Appendix B]:

$$\frac{\partial \rho}{\partial t} + \nabla \cdot (\rho \mathbf{v}) = 0, \tag{1}$$

$$\frac{\partial (\rho \phi)}{\partial t} + \nabla \cdot (\rho \mathbf{v} \phi + \mathbf{J}_\phi) = 0, \tag{2}$$

$$\frac{\partial (\rho \mathbf{v})}{\partial t} + \nabla \cdot (\rho \mathbf{v}\mathbf{v} + \mathbf{J}_v) = -\nabla p + \mathbf{F}_\phi, \tag{3}$$

$$\frac{\partial (\rho u)}{\partial t} + \nabla \cdot (\rho \mathbf{v} u + \mathbf{J}_u) = -p \nabla \cdot \mathbf{v} - \mathbf{J}_v : \nabla \mathbf{v} - \mathbf{J}_\phi \cdot \nabla \psi_{12}, \tag{4}$$

where ρ is the mixture density (which here is assumed to be constant), $\mathbf{v}$ is the mass-averaged fluid velocity, ϕ is the mass fraction of species *1*, p is pressure, and u is the specific (i.e., per unit mass) internal energy of the mixture. The terms $\mathbf{J}_\phi$, $\mathbf{J}_v$, and $\mathbf{J}_u$ represent the irreversible diffusive fluxes of species, momentum, and internal energy, respectively, while $\mathbf{F}_\phi$ is the volumetric body force exerted by any long-range conservative force acting on the two species (see Chap. 7.4 of Mauri [45] or Chap. II.3 of De Groot and Mazur [46]). In this specific case, where gravity and other conservative energy fields are neglected, $\mathbf{F}_\phi$ reduces to the Korteweg force, which is captured by the energy potential difference ψ_{12}, described later on in this section. The terms on the right-hand side (RHS) of Eq. (4) represent the volumetric heat source terms, which are strictly positive according to nonequilibrium thermodynamics (see Chap. 7.5 of Mauri [45]). It is worth noting that the first term on the RHS of Eq. (4), namely $-p \nabla \cdot \mathbf{v}$, is identically zero as a consequence of the assumption of constant density, which reduces the continuity equation [Eq. (1)] to $\nabla \cdot \mathbf{v} = 0$. In fact, in these conditions, pressure ceases to be a thermodynamic variable for incompressible fluids and acquires instead the ancillary status of mere gauge variable, enforcing the solenoidal nature of the velocity field.

In the balance of chemical species, Eq. (2), the diffusive mass flux of species *1*, $\mathbf{J}_\phi$, obeys the following constitutive relation [see Eqs. (B12) and (B16)]:

$$\mathbf{J}_\phi = -\frac{\rho D}{R_w T} \phi (1 - \phi) ([\nabla \mu_{12}]_T + \nabla \psi_{12}), \tag{5}$$

with $R_w = R/M_w$, where R is the gas constant, T is the absolute temperature, D is the molecular diffusivity, and $[\nabla \mu]_T = (\partial \mu / \partial \phi)_T \nabla \phi$, where we have denoted $\mu_{12} = \mu_1 - \mu_2$ and $\psi_{12} = \psi_1 - \psi_2$ as, respectively, the chemical potential difference and the potential energy difference of any conservative force acting on the components of the mixture. Note that, in the dilute limit (i.e., $\phi \to 0$ or $\phi \to 1$) and for ideal mixtures ($\Psi = 0$ and $\psi_{12} = 0$), Fick law is correctly recovered in Eq. (5) (see discussion at the end of Appendix B).

In the momentum balance, Eq. (3), the viscous momentum flux $\mathbf{J}_v$ is symmetric, as we assume that no body couples are applied to the system. The viscous momentum flux $\mathbf{J}_v$ is linked to the

commonly used stress tensor $\mathbf{T}$ as $\mathbf{T} = \mathbf{J}_v + p\mathbf{I}$ [18], where $\mathbf{I}$ is the identity tensor; in addition, $\mathbf{J}_v$ can be decomposed as the sum of an isotropic and a deviatoric part, i.e., $\mathbf{J}_v = p'\mathbf{I} + \mathbf{J}'_v$, where p' is a dynamical (i.e., nonthermodynamic) pressure term, while $\mathbf{J}'_v$ is the traceless part of the stress tensor (see Chap. 7.5 of Mauri [45]). Applying the rules of nonequilibrium thermodynamics (see Appendix B), we obtain the constitutive relations for a Newtonian fluid, that is, $p' = -\zeta\nabla\cdot\mathbf{v}$ [see Eq. (B7)] and $\mathbf{J}'_v = -\eta(\nabla\mathbf{v} + \nabla\mathbf{v}^{\mathrm{T}} - \frac{2}{3}(\nabla\cdot\mathbf{v})\mathbf{I})$ [see Eq. (B10)], where η is the mixture dynamic viscosity and ζ is the bulk viscosity. Thus, finally we obtain:

$$\mathbf{J}_v = -\eta(\nabla\mathbf{v} + \nabla\mathbf{v}^{\mathrm{T}}) - \left(\zeta - \tfrac{2}{3}\eta\right)(\nabla\cdot\mathbf{v})\mathbf{I}. \tag{6}$$

Naturally, in Eq. (6) the isotropic term proportional to $(\nabla\cdot\mathbf{v})\mathbf{I}$ can be dropped because the velocity field is solenoidal (i.e., $\nabla\cdot\mathbf{v} = 0$) for an incompressible mixture.

In Eq. (3) the body force $\mathbf{F}_\phi$, which captures the nonlocal effects induced by a long-range conservative force, is denoted as Korteweg force and has the form [see Appendix C, in particular Eq. (C8)]:

$$\mathbf{F}_\phi = -\rho\phi\nabla\psi_{12}, \tag{7}$$

where a pressure-like term has been dropped [18,43,47] and the potential energy difference is linked to the mass fraction field as [see Eq. (C7)]:

$$\psi_{12} = -R_w T a^2\nabla^2\phi, \tag{8}$$

with a denoting the characteristic length of the diffuse interface. As a common practice in phase-field modeling [18], only the leading-order term $\nabla^2\phi$ in the gradient expansion is considered because the higher-order terms (i.e., fourth and beyond) provide only a negligible contribution to the dynamics of phase separation [48]; thus, the applicability of the model extends even far from critical conditions.

The magnitude of the Korteweg force and, in turn, the characteristic length a are not arbitrary quantities but, rather, are linked to mixture thermodynamics, in particular to the equilibrium surface tension of the two phases. Consistently with the Cahn-Hilliard framework [20], ψ_{12} vanishes within the bulk of each phase; in addition, imposing that the excess energy stored at equilibrium per unit area of the interface is the surface tension σ, we find, near the critical point [14],

$$\sigma = \kappa\rho R_w T a, \tag{9}$$

where κ is the dimensionless magnitude of the line integral of the thermodynamic excess free energy across the interfacial region at equilibrium [49]. Based on the results of Lamorgese and Mauri [50], we have

$$\kappa = \frac{f}{2}(\Psi - 2)^{3/2}, \tag{10}$$

where $f = 1 - 0.6515(\Psi-2) + 0.29879(\Psi-2)^2 - 0.07928(\Psi-2)^3 + 0.0087(\Psi-2)^4$ interpolates Fig. 2 of Lamorgese and Mauri [50] for $2 \leqslant \Psi \leqslant 5$, where Ψ is the Margules parameter. It should be noted that, in Lamorgese and Mauri [50] as well as in previous publications of the authors, a factor 4 was erroneously used in Eq. (10) instead of the denominator 2. In general, far from the critical point, we have $\kappa = O(10^{-1})$; for example, when $\Psi = 3$, we find $\kappa \approx 0.3$ while, closer to the critical point, κ gets smaller, for example being $\kappa \approx 0.015$ when $\Psi = 2.1$. Finally, for a van der Waals fluid the characteristic length a scales with temperature as [18]

$$a = \hat{a}\sqrt{\frac{T_c}{T}}, \tag{11}$$

where $\hat{a}$ is a temperature-independent characteristic length and T_c represents the critical temperature of the mixture. Note that Eq. (11) implies that a^2T is constant (see the end of Appendix C), thus, according to Eq. (8), the conservative force is temperature independent (i.e., $\partial\psi_{12}/\partial T = 0$), which

means that the gradient of the potential energy difference in both Eqs. (5) and (7) is actually $\nabla\psi_{12} = \frac{\partial\psi_{12}}{\partial\phi}\nabla\phi = [\nabla\psi_{12}]_T$.

In the energy balance, Eq. (4), the constitutive equation for the diffusive heat flux $\mathbf{J}_u$ takes into account both the conductive contribution to heat flux according to Fourier law and the enthalpic contribution associated to species flux [see Eqs. (B9) and (B14)]:

$$\mathbf{J}_u = -k\nabla T + \bar{h}_{12}\mathbf{J}_\phi, \tag{12}$$

where k is the thermal conductivity of the mixture and $\bar{h}_{12}$ is the partial mass enthalpy difference.

Throughout the section it is evident how the thermodynamic properties of the mixture are intertwined with the constitutive expressions of fluxes [for example, Eqs. (5) and (12)] and other physical quantities (e.g., the diffuse interface length a in Eq. (11) and its implications on the Korteweg force and surface tension in Eqs. (7)–(10)). Therefore, the whole diffuse interface approach would have little physical ground without a consistent thermodynamic framework. The thermodynamics of regular and symmetric binary mixtures is reported in Appendix A, from which key results are reported in the following in order to provide closure expressions to the model. In particular, the chemical potential difference, the partial enthalpy difference, and the internal energy (all of them per unit mass) result as follows:

$$\mu_{12} = R_w T \ln\left(\frac{\phi}{1-\phi}\right) + R_w T \Psi(1-2\phi), \tag{13}$$

$$\bar{h}_{12} = R_w T \Psi(1-2\phi), \tag{14}$$

$$u = c(T - T_{\mathrm{ref}}) + R_w T \Psi\phi(1-\phi), \tag{15}$$

where c is specific heat of the mixture and T_{ref} is an arbitrary reference temperature (which can be conveniently taken as $T_{\mathrm{ref}} = T_c$). The Margules parameter Ψ, which captures the nonideal behavior of the mixture and triggers phase separation for $\Psi > 2$, is linked to T and T_c as follows:

$$\Psi = \frac{2T_c}{T}. \tag{16}$$

In general, the physical properties of the mixture, such as diffusivity, viscosity, thermal conductivity, and heat capacity, depend on composition ϕ and temperature T (or, equivalently, on its inverse, i.e., Ψ, via Eq. (16)); therefore, we define

$$\rho(\Psi,\phi) = \hat{\rho}\times 1; \quad D(\Psi) = \hat{D}\times\tilde{D}(\Psi); \quad \eta(\Psi,\phi) = \hat{\eta}\times\tilde{\eta}(\Psi,\phi)$$
$$k(\Psi,\phi) = \hat{k}\times\tilde{k}(\Psi,\phi); \quad c(\Psi,\phi) = \hat{c}\times\tilde{c}(\Psi,\phi), \tag{17a–17e}$$

where quantities with hats are dimensional and indicate typical values of that specific physical quantity (for example, $\hat{D} = 10^{-9}\,\mathrm{m}^2/\mathrm{s}$), while their counterparts with tildes are O(1) nondimensional functions of temperature and composition.

B. Boundary and initial conditions

The governing equations, i.e., Eqs. (1)–(4), are strongly coupled. For example, the velocity field determines the composition and the energy field, and, in turn, it is determined by the composition field via the Korteweg body force (see discussion in Chueh *et al.* [43]). The system of Eqs. (1)–(4) is solved here in 2D within a rectangular box with $x \in [0, W]$ and $y \in [-H, H]$, where W and H denote the domain length and semiheight, respectively. Periodic conditions of $\mathbf{v}$, ϕ, p, and T are applied at $x = 0$ and $x = W$, while at the horizontal boundaries ($y = \pm H$) we impose: (i) a constant shear rate with $\mathbf{v}(y = \pm H) = \pm\gamma H\mathbf{e}_x = \pm v_H\mathbf{e}_x$, where $\mathbf{e}_x$ is the unit vector in the x direction, γ is the unperturbed shear rate, and $v_H = \gamma H$ is the corresponding velocity magnitude; physically, this means having two plates at a distance $2H$ moving in opposite directions, with no fluid slip at the wall; (ii) no species mass flux condition [i.e., $\mathbf{e}_y \cdot (\rho\mathbf{v}\phi + \mathbf{J}_\phi) = \mathbf{e}_y \cdot \mathbf{J}_\phi = 0$] and same wettability for

the two phases, corresponding to a 90° contact angle (i.e., $\mathbf{e}_y \cdot \nabla\phi = 0$) [15,44]; consequently, we obtain the following boundary conditions: $\partial\phi/\partial y(y = \pm H) = 0$ and $\partial^3\phi/\partial y^3(y = \pm H) = 0$; and (iii) imposed temperature $T(y = \pm H) = T^{\pm}$, with $T^{\pm} < T_c$.

As initial condition, we impose uniform velocity $\mathbf{v} = \mathbf{0}$ (i.e., the fluid is still), pressure $p = p_0$, and temperature $T = T_0$, with $T_0 > T_c$, and a uniform mass fraction $\phi_0 \in (0, 1)$ is considered throughout the domain along with a superimposed small random white noise, $\varepsilon = \delta\phi$, with $\langle\varepsilon\rangle = 0$ and $\langle\varepsilon^2\rangle^{1/2} = 10^{-2}$ at $t = 0$. According to these conditions, mass and chemical species are conserved while energy is not conserved, tending to decrease and flowing out of the simulation domain (at least, until a statistically stationary configuration is reached).

C. Governing equations in dimensionless form

The governing equations (1)–(4) are recast in dimensionless form using the following scaling:

$$\tilde{\mathbf{x}} = \frac{\mathbf{x}}{\hat{a}}, \quad \tilde{t} = \frac{\hat{D}}{\hat{a}^2}t, \quad \tilde{\mathbf{v}} = \frac{\hat{a}}{\hat{D}}\mathbf{v}, \quad \tilde{T} = \frac{T}{T_c} = \frac{2}{\Psi}, \tag{18a–18d}$$

where the characteristic interface thickness $\hat{a}$ is used as length scale, the diffusion characteristic time $\hat{a}^2/\hat{D}$ as timescale, the diffusion velocity $\hat{D}/\hat{a}$ as a characteristic speed, and temperature is scaled in terms of its critical value, using the Margules parameter Ψ. In particular, the Margules parameter Ψ is considered as a dependent variable in place of temperature. Consequently, the pressure and the internal energy scale as $p = (\hat{\eta}\hat{D}/\hat{a}^2)\tilde{p}$ and $u = 2\hat{c}T_c\tilde{u}$, while the fluxes of momentum, chemical species, and heat scale as $\mathbf{J}_v = (\hat{\eta}\hat{D}/\hat{a}^2)\tilde{\mathbf{J}}_v$, $\mathbf{J}_\phi = (\hat{\rho}\hat{D}/\hat{a})\tilde{\mathbf{J}}_\phi$, and $\mathbf{J}_u = (2\hat{k}T_c/\hat{a})\tilde{\mathbf{J}}_u$.

Following this scaling, we obtain the following dimensionless equations:

$$\tilde{\nabla}\cdot\tilde{\mathbf{v}} = 0, \tag{19}$$

$$N_{\mathrm{Sc}}^{-1}\left(\frac{\partial\tilde{\mathbf{v}}}{\partial\tilde{t}} + \tilde{\mathbf{v}}\cdot\tilde{\nabla}\tilde{\mathbf{v}}\right) + \tilde{\nabla}\cdot\tilde{\mathbf{J}}_v = -\tilde{\nabla}\tilde{p} + N_\alpha\phi\tilde{\nabla}(\tilde{\nabla}^2\phi), \tag{20}$$

$$\left(\frac{\partial\phi}{\partial\tilde{t}} + \tilde{\mathbf{v}}\cdot\tilde{\nabla}\phi\right) + \tilde{\nabla}\cdot\tilde{\mathbf{J}}_\phi = 0, \tag{21}$$

$$N_{\mathrm{Le}}^{-1}\left(\frac{\partial\tilde{u}}{\partial\tilde{t}} + \tilde{\mathbf{v}}\cdot\tilde{\nabla}\tilde{u}\right) + \tilde{\nabla}\cdot\tilde{\mathbf{J}}_u = -\frac{1}{2}N_\alpha^{-1}N_{\mathrm{Le}}^{-1}N_c^{-1}\tilde{\mathbf{J}}_v : \tilde{\nabla}\tilde{\mathbf{v}} + \frac{1}{2}N_{\mathrm{Le}}^{-1}N_c^{-1}\tilde{\mathbf{J}}_\phi\cdot\tilde{\nabla}(\tilde{\nabla}^2\phi), \tag{22}$$

where $\tilde{u} = \tilde{c}(\Psi^{-1} - 1/2) + N_c^{-1}\phi(1-\phi)$, with the following constitutive relations:

$$\tilde{\mathbf{J}}_v = -\tilde{\eta}(\tilde{\nabla}\tilde{\mathbf{v}} + \tilde{\nabla}\tilde{\mathbf{v}}^{\mathrm{T}}), \tag{23}$$

$$\tilde{\mathbf{J}}_\phi = -\tilde{D}\left((1 - 2\Psi\phi(1-\phi))\tilde{\nabla}\phi - \frac{\Psi}{2}\phi(1-\phi)\tilde{\nabla}(\tilde{\nabla}^2\phi)\right), \tag{24}$$

$$\tilde{\mathbf{J}}_u = \frac{\tilde{k}}{\Psi^2}\tilde{\nabla}\Psi + N_{\mathrm{Le}}^{-1}N_c^{-1}(1 - 2\phi)\tilde{\mathbf{J}}_\phi. \tag{25}$$

Note that the continuity equation [i.e., $\tilde{\nabla}\cdot\tilde{\mathbf{v}} = 0$, Eq. (19)] has been enforced to simplify the dimensionless expressions in Eqs. (22) and (23) compared to their dimensional counterparts, Eqs. (4) and (6), respectively.

The governing equations are expressed in terms of the following independent nondimensional numbers which characterize the system:

$$N_{\mathrm{Sc}} = \frac{\hat{\eta}}{\hat{\rho}\hat{D}}, \quad N_{\mathrm{Le}} = \frac{\hat{k}}{\hat{\rho}\hat{c}\hat{D}}, \quad N_c = \frac{\hat{c}}{R_w}, \quad N_\alpha = \hat{\rho}R_wT_c\frac{\hat{a}^2}{\hat{\eta}\hat{D}}, \tag{26a–26d}$$

which are the Schmidt number, N_{Sc}, expressing the ratio between momentum diffusivity $(\hat{\eta}/\hat{\rho})$ and molecular diffusion $(\hat{D})$; the Lewis number, N_{Le}, indicating the ratio between heat diffusivity

$(\hat{k}/(\hat{\rho}\hat{c}))$ and molecular diffusion ($\hat{D}$); the dimensionless heat capacity, N_c, and the fluidity parameter, N_α, where the latter can be regarded as an intrinsic Péclet number or as the inverse of an intrinsic capillary number [43,51–53]. The fluidity parameter indicates whether the phase separation process is driven by mass diffusion ($N_\alpha \leqslant 1$) or by convection ($N_\alpha \gg 1$) [43,52]. For convenience, in the following we assume that mixtures having different values of N_α differ by the viscosity only (i.e., the smaller N_α, the larger $\hat{\eta}$).

Boundary and initial conditions are recast in dimensionless form as well. The 2D computational domain lies within $\tilde{x} \in [0, \tilde{W}]$ and $\tilde{y} \in [-\tilde{H}, \tilde{H}]$, with periodic boundary conditions at $\tilde{x} = 0$ and $\tilde{x} = \tilde{W}$, while at $\tilde{y} = \pm\tilde{H}$: (i) walls move in opposite directions, i.e., $\tilde{v}_x = \pm\tilde{\gamma}\tilde{H}$, where $\tilde{\gamma} = (\hat{a}^2/\hat{D})\gamma$ represents the dimensionless shear rate; (ii) no species mass flux, $\mathbf{e}_y \cdot (\tilde{\mathbf{v}}\phi + \tilde{\mathbf{J}}_\phi) = \mathbf{e}_y \cdot \tilde{\mathbf{J}}_\phi = 0$ and 90° contact angle, i.e., $\mathbf{e}_y \cdot \tilde{\nabla}\phi = 0$; and (iii) fixed temperature, $\Psi(\pm\tilde{H}) = \Psi^{\pm}$, with $\Psi^{\pm} > 2$. As initial conditions, we have $\tilde{\mathbf{v}} = \mathbf{0}$, $\tilde{p} = 0$, $\phi = \phi_0 + \varepsilon$, and $\Psi = \Psi_0 < 2$, representing a nonseparated homogeneous mixture at rest with small superimposed random noise on composition.

Finally, from the set of six independent nondimensional numbers (i.e., N_{Sc}, N_{Le}, N_c, N_α, $\tilde{\gamma}$, and $\tilde{H}$) characterizing the system, it is possible to define other important parameters, such as

$$N_{\mathrm{Re}} = \frac{\hat{\rho} v_H H}{\hat{\eta}} = \frac{\tilde{\gamma}\tilde{H}^2}{N_{\mathrm{Sc}}}, \quad N_{\mathrm{Pe}} = \frac{v_H H}{\hat{D}} = \tilde{\gamma}\tilde{H}^2, \quad N_{\mathrm{Ca}} = \frac{\hat{\eta} v_H}{\hat{\sigma}} = \frac{\tilde{\gamma}\tilde{H}}{N_\alpha}, \tag{27a–27c}$$

expressing the Reynolds number, the Péclet number, and the capillary number, respectively, where v_H is taken as characteristic fluid velocity and $\hat{\sigma} = \hat{\rho} R_w T_c \hat{a}$ is a representative surface tension.

In order to get a feeling of typical values characterizing the system, consider a low-viscosity liquid binary mixture as acetone-hexadecane; at $T = 293\,\mathrm{K}$ we have $\hat{\eta} \approx 1.2\times10^{-3}\,\mathrm{kg/(m\,s)}$, $\hat{\rho} \approx 0.8\times10^{3}\,\mathrm{kg/m^3}$, $\hat{D} \approx 1.2\times10^{-9}\,\mathrm{m^2/s}$, $\hat{k} \approx 0.18\,\mathrm{W/(m\,K)}$, $\hat{c} \approx 2.2\times10^{3}\,\mathrm{J/(kg\,K)}$, $M_w \approx 60\,\mathrm{g/mol}$, $R_w \approx 1.3\times10^{2}\,\mathrm{J/(kg\,K)}$, $T_c = 305\,\mathrm{K}$ and thus $\Psi = 2.08$. Consequently, we find $N_{\mathrm{Sc}} \approx 10^3$, $N_{\mathrm{Le}} \approx 10^2$, $N_c \approx 15$. Then, from Eq. (10) we get $\kappa \approx 10^{-2}$ and, with $\sigma \approx 3\times10^{-2}\,\mathrm{N/m}$, by combining Eqs. (9) and (11) we estimate the characteristic interface thickness as $\hat{a} \approx 10^{-7}$ m, thus resulting in $N_\alpha \approx 10^5$. More viscous mixtures will have smaller fluidity numbers. It is very important to observe that the characteristic thickness $\hat{a}$ is a mesoscale length, quite larger than the molecule-size. This is coherent with the fact that the basis of the phase-field approach is a coarse-grained energy functional [see Eq. (A1)], where local equilibrium is assumed. We conclude that, in practical applications of the phase-field scheme, the square-gradient coefficient a^2 of the capillary force in Eq. (8) should be determined from experimental surface tension data by applying Eqs. (9) and (10), as also discussed by Llovell *et al.* [54]; therefore, it would be quite wrong to treat $\hat{a}$ as a free parameter, as that would determine a physically inconsistent value of the surface tension.

D. Numerical implementation and parameters

As in previous works [43,44], we implemented the phase-field model in the commercial finite-element method code COMSOL MULTIPHYSICS v. 5.5 [55], so that using this model is not restricted to a small number of specialists but it is now readily available to a much wider audience. The mass and momentum balance [Eqs. (19) and (20)] are solved with the laminar flow interface, which basically solves the Navier-Stokes equation, where the Korteweg force [last term on the RHS of Eq. (20)] is implemented as a volumetric force. The conservation of species and energy [Eqs. (21) and (22)] are implemented by using the general form partial differential equation (PDE) interface, which requires an auxiliary field variable ($\tilde{w}$) and a corresponding auxiliary equation ($\tilde{w} = \tilde{\nabla}^2\phi$) to solve the resulting fourth-order differential equation [43,44].

The governing equations were simulated in a rectangular box with $\tilde{W} = 400$ and $\tilde{H} = 50$ if not otherwise specified, with a spatial discretization of one $\hat{a}$ unit, resulting in a uniform 100×400 computational mesh. Time is integrated with the default COMSOL MULTIPHYSICS settings, with a fully coupled approach with MUMPS direct solver, with a maximum time step of 20 dimensionless time units. Numerical tests have shown that, using these settings, results are stable and grid independent [44].

TABLE I. List of parameters used in each section in this study.

Parameter	Value			
	Sec. III A	Sec. III B	Sec. III C	Sec. III D
$\tilde{W}$	150	400	400	400
$\tilde{H}$	75	50	50	50
N_{Sc}	10^2	10^2	10^2	10^2
N_α	10^{-2}	10^{-2}–10^2	10^2	10^2
N_{Le}	10^{-1}–10^1	10^{-1}–10^1	10^1	10^1
N_c	∞	∞	10^{-3}–∞	∞
$\tilde{D} = \tilde{\eta} = \tilde{c}$	1	1	1	1
$\tilde{k}$	1	1	1	$0.1\times10^{\phi/0.4}$
$\tilde{\gamma}$	0	10^{-2}	10^{-2}	10^{-2}
Ψ^+	2.6	2.6	2.6	2.6
Ψ^-	2.1	2.1	2.1	2.1
Ψ_0	1.9	1.9	1.9	1.9
ϕ_0	0.4	0.4	0.4	0.4

Table I summarizes the values of the parameters used in this study. In all the simulations the initial mass fraction is set to $\phi_0 = 0.4$, which means that the phase rich in component 1 represents the minority phase; the initial Margules coefficient is set to $\Psi_0 = 1.9$, thus representing a homogeneous mixture at a temperature slightly above the critical temperature. The opposite walls at $\tilde{y} = \pm\tilde{H}$ are cooler than the critical temperature, thus triggering phase separation; a temperature gradient is imposed with $\Psi^+ = 2.6$ and $\Psi^- = 2.1$. The dimensionless shear rate is set to $\tilde{\gamma} = 10^{-2}$, representing a case of intermediate shear as for our previous study [43]. The Schmidt number is set to $N_{\mathrm{Sc}} = 10^2$; thus, according to Eq. (27a), the Reynolds number is $N_{\mathrm{Re}} = 0.25$, indicating that the flow regime is laminar. The Lewis and fluidity numbers are varied between $N_{\mathrm{Le}} = 10^{-1}$–$10^1$ and $N_\alpha = 10^{-2}$–10^2 in order to account for opposite behaviors of the system upon changes in thermal conductivity and viscosity, respectively. The effect of the dimensionless heat capacity N_c is investigated as well, letting it range between 10^{-3} and infinity. With these settings, simulations span a wide range of capillary numbers ($N_{\mathrm{Ca}} = 5\times10^{-3} - 5\times10^1$), being it below or above the critical capillary number $N_{\mathrm{Ca}}^{cr} \approx O(10^{-1})$ [13]. The dimensionless physical properties of the fluid, which are functions of temperature and composition, are set to $\tilde{D} = \tilde{\eta} = \tilde{k} = \tilde{c} = 1$ if not explicitly mentioned. At least two simulations with different initial distribution of the random noise ε are performed for each parametric setting.

III. RESULTS AND DISCUSSION

A. Case of no shear: Model verification

Before addressing the dynamics of phase separation under shear flow of a nonisothermal binary mixture, the model is validated in the limit case of no imposed shear and in the limit of infinite heat capacity (i.e., $N_c^{-1} = 0$) and low fluidity number (namely, $N_\alpha = 10^{-2}$). In this condition, convection and momentum transport play no role as phase separation is ruled by mass diffusion and proceeds according to thermal conduction under a temperature gradient, thus replicating the scenario simulated by Bertei *et al.* [44]. Figure 1 shows representative snapshots of the evolution of phase separation for two different values of the Lewis number, $N_{\mathrm{Le}} = 0.1$ and $N_{\mathrm{Le}} = 10$; as such, results in Fig. 1 replicate the snapshots reported in Fig. 8 of Bertei *et al.* [44], the only exception being that in the present study the temperature gradient is applied in the vertical direction (with Ψ^+ at the top) while in Bertei *et al.* [44] the temperature gradient is oriented horizontally (with Ψ^+ on

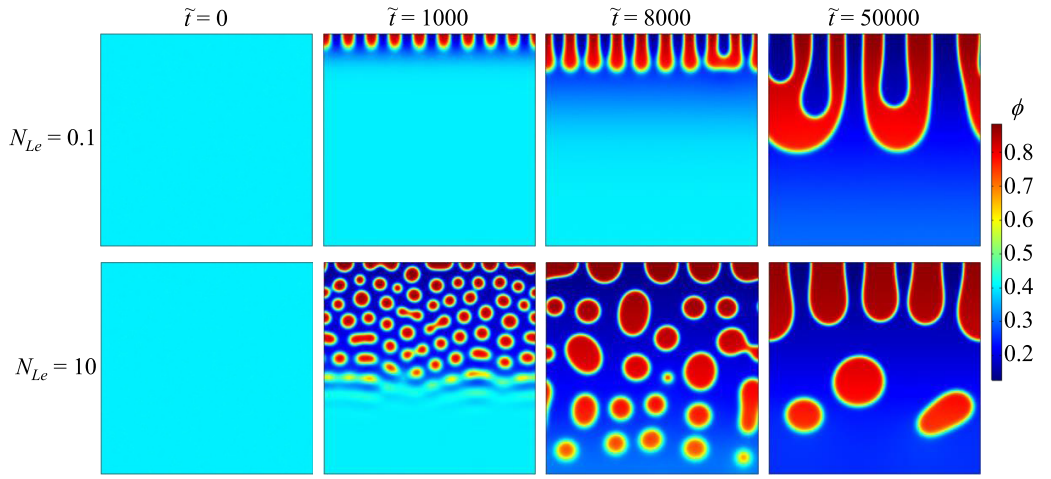

FIG. 1. Phase separation of a binary mixture at different dimensionless times under a thermal gradient in the limit case of no imposed shear (i.e., $\tilde{\gamma} = 0$) at $N_\alpha = 10^{-2}$ and $N_c^{-1} = 0$ for two values of the Lewis number. In these simulations a square domain with $\tilde{W} = 150$ is used. The other parameters, kept constant throughout this study if not otherwise specified (see Table I), are $N_{\mathrm{Sc}} = 10^2$, $\Psi^+ = 2.6$, $\Psi^- = 2.1$, $\Psi_0 = 1.9$, $\phi_0 = 0.4$, $\tilde{D} = \tilde{\eta} = \tilde{c} = \tilde{k} = 1$.

the right). For a detailed description of phase separation under a temperature gradient in the absence of convection, the reader is referred to our previous study [44].

Figure 1 shows that at $\tilde{t} = 0$ the mixture is homogeneous, with a uniform composition $\phi = 0.4$ (light blue color; see the scale bar of mass fraction on the right side of Fig. 1). For $N_{\mathrm{Le}} = 0.1$ heat conduction is comparatively slower than mass diffusion; thus, phase separation starts from the cooler wall at the top, where the first droplets of the minority phase (i.e., rich in component 1, in red) emerge for $\tilde{t} \approx 1000$, separated by regions rich in component 2 (in blue). Phase separation proceeds at the same pace of the (slower) temperature progression front, forming elongated stripes of the component 1-rich phase which grow with time and coalesce laterally as the tips merge into one another at $\tilde{t} \approx 50\,000$. On the other hand, for $N_{\mathrm{Le}} = 10$ heat conduction is faster than mass diffusion, so that the temperature field is rapidly established; then, droplets of the minority phase nucleate first close to the cooler wall at the top, being such a nucleation initially independent from the evolution of the nearby droplets. A propagation front of nucleating droplets proceeds from top to bottom, with patches of the red phase (which is rich in component 1) merging into each other according to Ostwald ripening for $\tilde{t} > 1000$, finally approaching a steady-state configuration consisting of stripes oriented along the temperature gradient (see the elongated droplets attached to the upper wall at $\tilde{t} = 50\,000$ for $N_{\mathrm{Le}} = 10$ in Fig. 1). In both cases, since the capillary number is zero, there are no breakups and droplets keep growing with time until steady state is reached.

Both these evolutions, which show remarkable differences in phase separation dynamics, are in excellent quantitative agreement with Fig. 8 of Bertei *et al.* [44], thus providing a consistent verification of the numerical model herein presented.

B. The role of capillary number and Lewis number

After its numerical validation shown in the previous section, the model is used to simulate non-isothermal phase separation under an imposed shear. From now on the dimensionless shear rate is set to $\tilde{\gamma} = 10^{-2}$, which represents a case of intermediate shear according to our previous investigation [43]. In these simulations, the upper wall moves to the right while the lower wall moves to the left; the imposed, unperturbed velocity profile (i.e., before the start of phase separation) is reported in

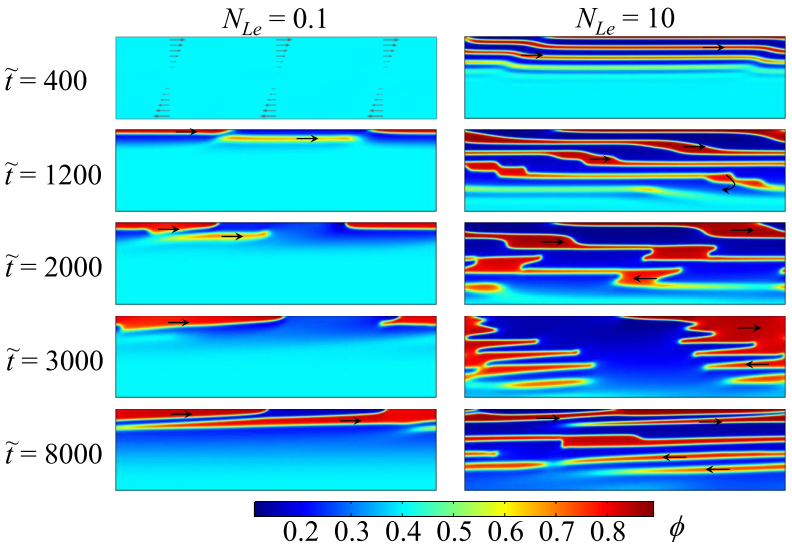

FIG. 2. Phase separation of a binary mixture having a high capillary number ($N_{\mathrm{Ca}} = 50 > N_{\mathrm{Ca}}^{cr}$) under a thermal gradient for an imposed dimensionless shear rate $\tilde{\gamma} = 10^{-2}$ for two values of the Lewis number (left and right panels). The fluidity number is set to $N_\alpha = 10^{-2}$ while $N_c^{-1} = 0$. The first snapshot reports the imposed velocity profile with gray arrows. In all the other snapshots, the black arrows are used to guide the eye to schematically indicate the direction of the red phase while it moves.

the left panel of Fig. 2 at $\tilde{t} = 400$ with gray arrows. Different values of the fluidity number (i.e., $N_\alpha = 10^{-2}$ or $N_\alpha = 10^2$) and Lewis number (i.e., $N_{\mathrm{Le}} = 0.1$ or $N_{\mathrm{Le}} = 10$) are investigated in this section to showcase the characteristic patterns of phase separation for different capillary numbers and different ratios between the rate of heat and mass diffusion. In all these simulations, an infinite value of the dimensionless heat capacity is considered (i.e., $N_c^{-1} = 0$).

The dynamics of phase separation for capillary number well beyond the critical value (namely, $N_{\mathrm{Ca}} = 50$) is shown in Fig. 2 for two characteristic values of the Lewis number by setting $N_\alpha = 10^{-2}$. In these conditions, equilibrated round droplets would be unstable as the shear would stretch them, finally leading to breakup [13,43]. Figure 2 (left panel) shows that, for $N_{\mathrm{Le}} = 0.1$, phase separation starts from the cooler upper wall at $\tilde{t} = 1200$. Elongated stripes of the red phase, rich in component 1, nucleate close to the upper wall and stretch moving to the right, that is, in the same direction of the imposed flow field as indicated by the black arrows, which are used throughout the study to guide the eye to schematically represent the movement of the red phase. As already described in the previous section, thermal conduction is slower than mass diffusion for $N_{\mathrm{Le}} = 0.1$, thus phase separation is triggered as soon as the temperature falls below the critical temperature (or, equivalently, as soon as $\Psi > 2$) along the height of the domain. As the cold temperature front moves downward with time, the width of the elongated stripes widens while the stripes keep their orientation, aligned with the flow field.

The case with $N_{\mathrm{Le}} = 10$ shows some similarities as well as some differences. Figure 2 (right panel) shows that phase separation starts from the cooler upper wall by forming stripes aligned with the velocity field, exactly as for the case of $N_{\mathrm{Le}} = 0.1$. However, since $N_{\mathrm{Le}} > 1$, heat diffuses faster than species, so that Ψ gets larger than 2 throughout the whole domain height for $\tilde{t} \approx 1200$. Notably, since the stripes are horizontal and aligned with the velocity field, heat is transported only by conduction along the vertical direction. The stripes formed at the top move rightward and widen vertically with time (compare $\tilde{t} = 400$ with $\tilde{t} = 1200$); as soon as they reach the center of the domain, where the velocity field swaps its orientation, the movement of the red stripes changes orientation too, as shown by the curved arrow at $\tilde{t} = 1200$. Therefore, the system is characterized by

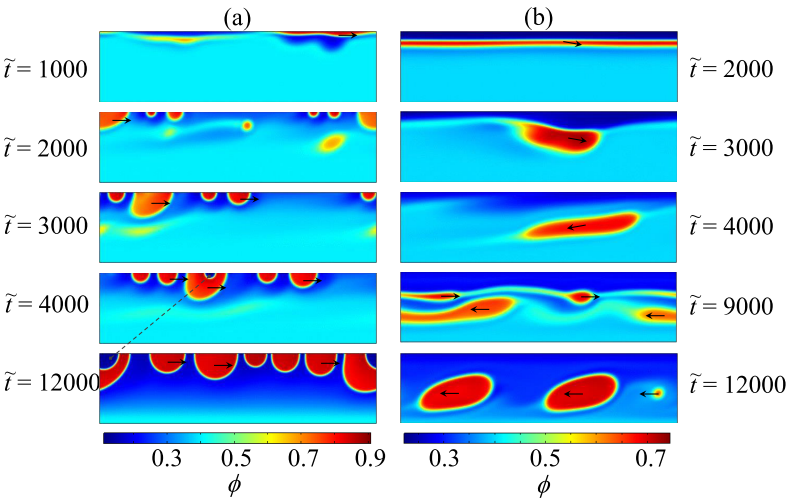

FIG. 3. Phase separation of a binary mixture having a small capillary number ($N_{\mathrm{Ca}} = 5\times10^{-3} < N_{\mathrm{Ca}}^{cr}$) under a thermal gradient for an imposed dimensionless shear rate $\tilde{\gamma} = 10^{-2}$ for $N_{\mathrm{Le}} = 0.1$. The fluidity number is set to $N_\alpha = 10^2$ while $N_c^{-1} = 0$. The two panels report two different evolutions depending on whether phase separation starts with nucleation at the top of the minority phase (a) or of the majority phase (b).

two series of horizontal stripes, with the upper ones moving to the right and the lower ones moving to the left (see the snapshot at $\tilde{t} = 2000$). Since the stripes widen vertically according to Ostwald ripening, they may temporarily coalesce into blobs (see the snapshot at $\tilde{t} = 3000$) which, however, are stretched and break up again into horizontal stripes because N_{Ca} is larger than the critical capillary number. The final configuration (Fig. 2, $\tilde{t} = 8000$, right panel) is thus made of horizontal stripes, moving in opposite directions, whose average width is determined by the balance between the vertical Ostwald ripening and the horizontal shear-induced breakup. Notably, such a system evolution for $N_{\mathrm{Le}} > 1$ under a temperature gradient is similar to that obtained in an instantaneous quench, as shown in Fig. 3 of our previous study [43].

Setting the fluidity parameter N_α equal to 10^2 produces two effects: (i) phase separation becomes dominated by convection instead of diffusion [43,52] and, more importantly, (ii) the capillary number falls to 5×10^{-3} according to Eq. (27c). Since N_{Ca} is smaller than the critical capillary number, which is $N_{\mathrm{Ca}}^{\mathrm{cr}} \approx O(10^{-1})$ [13,43,56], an equilibrated droplet would remain stable under the shear, without breaking up. Figure 3 illustrates the dynamics of phase separation in this condition when $N_{\mathrm{Le}} = 0.1$; in particular, the two cases of system evolution are reported in panels 3(a) and 3(b), respectively.

Since $N_{\mathrm{Le}} < 1$, heat diffuses vertically slower than mass, so the system cools down slowly from the upper wall, triggering spinodal decomposition. Since the wettability of the two components with the wall is the same (see Sec. II B) and considering that patches of the two phases nucleate at the wall and align horizontally by following the velocity field, it may happen that either the first layer is mainly composed by the minority phase (i.e., component 1, in red) as in Fig. 3(a) for $\tilde{t} = 1000$ or that the first layer is made of the other phase (i.e., component 2, in blue) as in Fig. 3(b) for $\tilde{t} = 2000$. Considering that the mass fraction is $\phi_0 = 0.4$, we may argue that such starting configurations happen with a probability equal to 40% for the first case and 60% for the second one. Depending on such a starting configuration and recalling that $N_{\mathrm{Ca}} < N_{\mathrm{Ca}}^{\mathrm{cr}}$, the following evolution of the system is determined. In the first case [Fig. 3(a)], the elongated red stripe at the upper wall evolves into a collection of droplets attached at the upper wall [Fig. 3(a), $\tilde{t} = 2000$]. In fact, for $N_{\mathrm{Ca}} < N_{\mathrm{Ca}}^{\mathrm{cr}}$ capillary forces are strong enough to keep the droplets as round as possible to minimize the interfacial energy [43,57]. Thus, the red droplets move coherently with the wall

($\tilde{t} = 3000$) and simultaneously grow as the system progressively cools down ($\tilde{t} = 4000$), eventually even merging together when they touch each other. Notably, drops of the blue phase can nucleate inside the red droplets and slowly grow with time according to Ostwald ripening as the system equilibrates (see the evolution of the blue drop identified by the dashed gray line between $\tilde{t} = 4000$ and $\tilde{t} = 12\,000$). Therefore, the final configuration of the system is represented by large droplets attached to the upper wall and moving coherently with it ($\tilde{t} = 12\,000$).

In the second case [Fig. 3(b)], the first layer nucleating from spinodal decomposition is mainly composed of component 2, thus pushing component 1 far from the upper wall [Fig. 3(b), $\tilde{t} = 2000$]. These two stripes widen according to Ostwald ripening as the system cools down from the top until capillary forces minimize the interfacial energy of the red stripe by forming a droplet of the minority phase ($\tilde{t} = 3000$), which drifts downward as the system cools down ($\tilde{t} = 4000$) similarly to what shown in Fig. 1 for $N_{\mathrm{Le}} = 0.1$. At $\tilde{t} = 4000$ the red droplet is placed at about the center of the domain and continues to drift downward, thus eventually changing orientation and moving to the left as soon as its center of mass falls below the centerline of the domain. Notably, the red droplet at $\tilde{t} = 4000$ is surrounded by a region of unseparated mixture (see the light blue color representative of $\phi = \phi_0 = 0.4$). As the system cools down from the top with time, spinodal decomposition is triggered from the upper regions of the domain and new droplets nucleate ($\tilde{t} = 9000$). These new droplets move to the right as they are placed in the upper part of the domain, eventually coalescing with the previously formed larger and stretched droplet ($\tilde{t} = 9000$), giving rise to bigger, rounder, and equilibrated droplets placed slightly off the centerline ($\tilde{t} = 12\,000$). Such a final configuration, featuring equilibrated droplets at about the center of the domain as in Fig. 3(b) at $\tilde{t} = 12\,000$, is different from the collection of droplets attached to the upper wall shown in Fig. 3(a) at $\tilde{t} = 12\,000$; these final configurations are basically the consequence of whether phase separation starts with the first layer composed by the minority phase [Fig. 3(a)] or not [Fig. 3(b)].

A remarkably different evolution of the system is obtained when $N_{\mathrm{Le}} = 10$, while still keeping $N_\alpha = 10^2$ and thus $N_{\mathrm{Ca}} = 5\times10^{-3} < N_{\mathrm{Ca}}^{\mathrm{cr}}$, as shown in Fig. 4. Since $N_{\mathrm{Le}} > 1$, the system cools down rapidly via conduction from the upper wall, thus triggering phase separation which generates the first patches of the minority and majority phases at the upper wall ($\tilde{t} = 200$). Since $N_{\mathrm{Ca}} < N_{\mathrm{Ca}}^{\mathrm{cr}}$, capillary forces quickly form round droplets ($\tilde{t} = 300$), which keep nucleating while moving to the right by following the flow field ($\tilde{t} = 400$). As the system keeps cooling down, the droplets drift downward towards the unseparated region ($\tilde{t} = 500$); however, as the red drops approach the centerline, the velocity field changes orientation, thus the drops change direction as well, moving to the left ($\tilde{t} = 600$ and $\tilde{t} = 700$). At $\tilde{t} = 800$ most of the red drops are below the domain centerline, thus moving to the left, the faster as the center of mass is closer to the lower wall. The collision among drops moving at different speed ($\tilde{t} = 900$), as well as the progressive cooling of the system, favors drop coalescence, which is evident by comparing the number and size of the drops at $\tilde{t} = 900$, 1000, and 1100. The final configuration (not shown) features large equilibrated droplets attached at the upper and lower walls moving in opposite directions.

Therefore, simulations results show that different values of the fluidity number (which in turn determines the capillary number) and Lewis number lead to completely different patterns of phase separation under a shear and a temperature gradient, spanning from elongated stripes moving with flow and potentially coalescing with each other, up to droplets moving and changing orientation within the bulk of the domain, with droplets that may even remain attached to the walls. All these different configurations are a consequence of the combination of a shear flow and an orthogonal temperature gradient.

C. The role of the dimensionless heat capacity

In all the previous sections the phase separation dynamics was simulated by considering an infinite dimensionless heat capacity, which was taken into account by setting $N_c^{-1} = 0$. According to the definition of N_c [Eq. (26c)], this situation applies to liquid mixtures of polymer melts or,

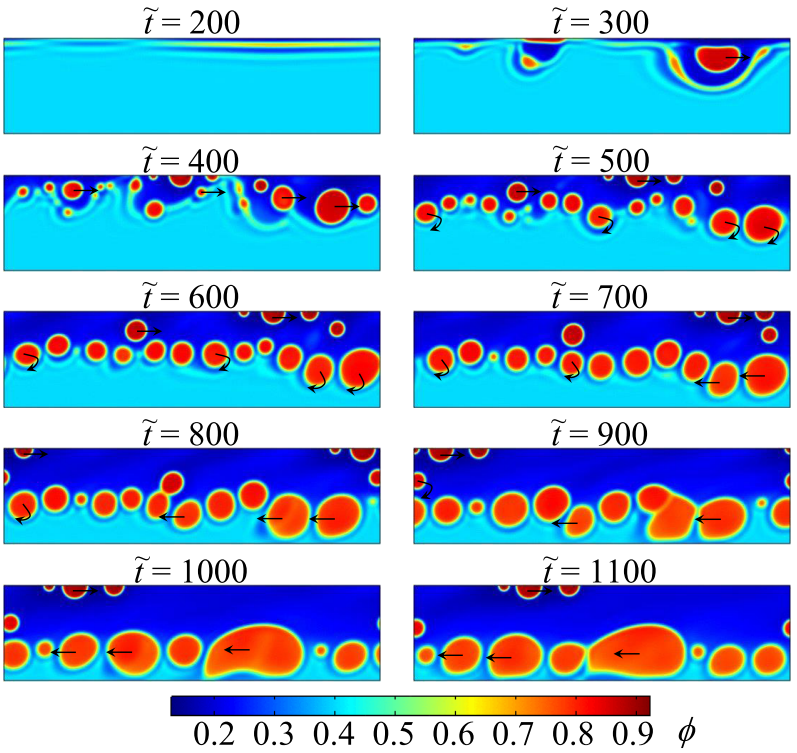

FIG. 4. Phase separation of a binary mixture having a small capillary number ($N_{\mathrm{Ca}} = 5\times10^{-3} < N_{\mathrm{Ca}}^{\mathrm{cr}}$) under a thermal gradient for an imposed dimensionless shear rate $\tilde{\gamma} = 10^{-2}$ for $N_{\mathrm{Le}} = 10$. The fluidity number is set to $N_\alpha = 10^2$ while $N_c^{-1} = 0$.

more generally, made by components with high molecular weight [32,44]. Such a simplification is removed in this section, where phase separation is simulated under a shear and a thermal gradient for different values of N_c (from 0.001 up to 100). The reference conditions replicate those used in Fig. 4, that is, $N_\alpha = 10^2$ and $N_{\mathrm{Le}} = 10$, corresponding to a system characterized by $N_{\mathrm{Ca}} < N_{\mathrm{Ca}}^{\mathrm{cr}}$ where heat conduction is faster than mass diffusion.

Figure 5 compares two representative snapshots of the system evolution, at $\tilde{t} = 600$ (left panel) and $\tilde{t} = 1500$ (right panel) for different values of the dimensionless heat capacity. The figure shows that as N_c decreases there is a delay in phase separation dynamics. In fact, for high values of N_c approaching the limit condition $N_c^{-1} \to 0$ (e.g., $N_c = 100$ down to $N_c = 1$), at $\tilde{t} = 600$ droplets of the minority phase have already nucleated in the upper part of the domain, drifting downward and then changing their orientation following the flow field, exactly as described in the previous section for Fig. 4. On the other hand, for smaller values of N_c, such as $N_c = 0.1$ or $N_c = 0.01$, phase separation lags behind at $\tilde{t} = 600$, with fewer and smaller droplets moving rightward in the top part of the domain (i.e., close to the cooler boundary). As N_c decreases further to $N_c = 0.001$, there is no distinct evidence of phase separation. The delay in phase separation dynamics as N_c decreases is even more evident at $\tilde{t} = 1500$ (right panel): the droplets are much larger and located in the lower part of the domain for $N_c = 100$ compared to $N_c = 0.1$, while for $N_c = 0.001$ there are no droplets at all.

The explanation for the delay in phase separation dynamics as N_c decreases stems from the role of the heat capacity in the energy equation, in particular in the source term on the RHS of Eq. (22). The source term is positive because, according to Eqs. (23) and (24), both $-\tilde{\mathbf{J}}_v : \tilde{\nabla}\tilde{\mathbf{v}} \geqslant 0$ and $\tilde{\mathbf{J}}_\phi \cdot \tilde{\nabla}(\tilde{\nabla}^2\phi) \geqslant 0$. From a physical perspective, such a source term represents the dissipation

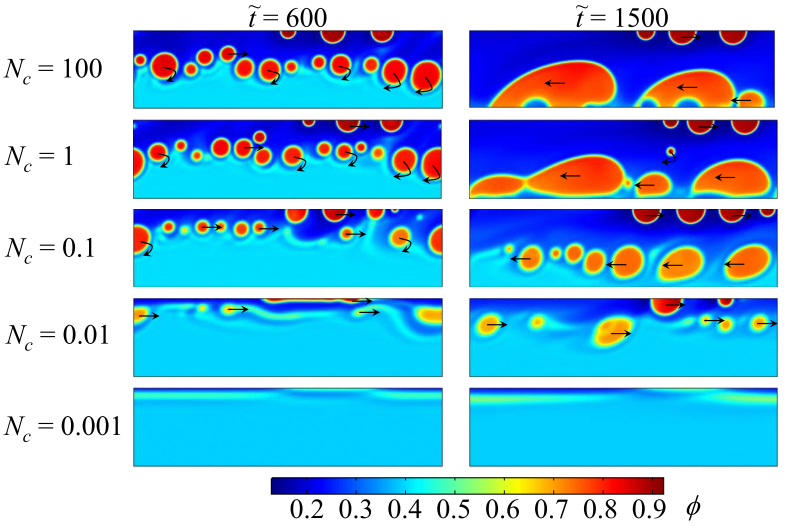

FIG. 5. Phase separation of a binary mixture under a thermal gradient for different values of the dimensionless heat capacity N_c at two representative times. The imposed dimensionless shear rate is $\tilde{\gamma} = 10^{-2}$ while $N_{\mathrm{Le}} = 10$ and $N_\alpha = 10^2$, corresponding to $N_{\mathrm{Ca}} = 5\times10^{-3} < N_{\mathrm{Ca}}^{\mathrm{cr}}$.

of energy into heat, which is indeed strictly positive according to nonequilibrium thermodynamics (see Chap. 7.5 of Mauri [45]). The source term depends linearly on N_c^{-1}, therefore, as N_c decreases, the magnitude of the source term increases, meaning that energy dissipation into heat causes an increase in the system internal energy and so of the system temperature as well. In this condition, despite the cooling of the system via the upper and lower boundaries, the internal heat production increases the system temperature, so Ψ may remain smaller than 2, without triggering spinodal decomposition. This is represented in Fig. 6(a), which compares the distribution of the Margules parameter Ψ at two representative times ($\tilde{t} = 600$ in the left panel and $\tilde{t} = 1500$ in the right panel)

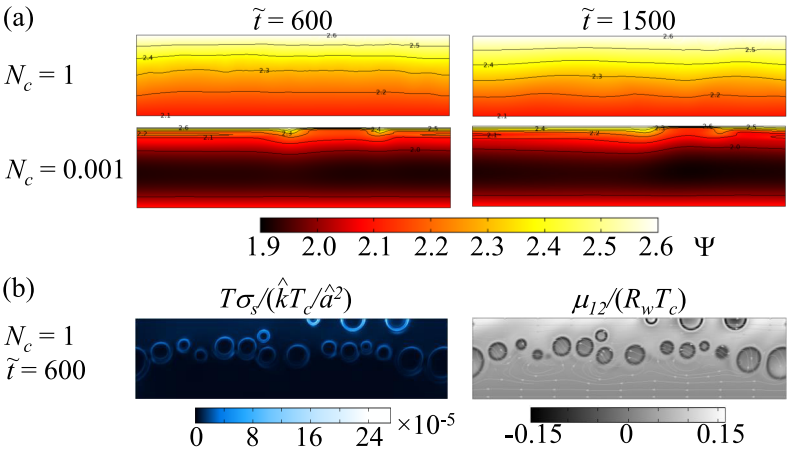

FIG. 6. (a) Distribution of the Margules parameter Ψ for two different values of the dimensionless heat capacity N_c at two representative times for $\tilde{\gamma} = 10^{-2}$, $N_{\mathrm{Le}} = 10$ and $N_\alpha = 10^2$, which are the same conditions as in Fig. 5; (b) dimensionless entropy production term and chemical potential difference, with superimposed velocity streamlines, for the case $N_c = 1$ at $\tilde{t} = 600$.

for two values of the dimensionless heat capacity. Figure 6(a) shows that for $N_c = 1$ the source term in the heat equation is relatively small so that Ψ is larger than 2 across the whole domain; thus, phase separation can start following the evolution described in Fig. 5. On the other hand, for $N_c = 0.001$ a large central portion of the domain is characterized by $\Psi \leqslant 2$, meaning that due to the internal heat production a large fraction of the domain cannot be cooled below the critical temperature. Accordingly, no phase separation is observed in Fig. 5 for $N_c = 0.001$. It is worth nothing that, in both cases, since the flux expressions follow nonequilibrium thermodynamics, the entropy production term [see Eq. (B6) in Appendix B] is strictly positive, meaning that the system evolves following the second law of thermodynamics. In particular, for the case undergoing phase separation, i.e., $N_c = 1$, the first panel in Fig. 6(b) shows that the dimensionless entropy production term $T\sigma_s/(\hat{k}T_c/\hat{a}^2)$ is positive everywhere, being larger at the droplet interfaces where the dimensionless chemical potential difference $\mu_{12}/(R_w T_c)$ experiences steep gradients [Fig. 6(b), second panel]. In fact, the main source of irreversibility arises from the entropy production at the interfaces, while the entropy production due to temperature gradients [which are mild according to Fig. 6(a)] and viscous dissipations [which are mild too according to the smooth velocity streamlines in Fig. 6(b), second panel] are negligible.

Therefore, the model is able to capture the effect of different values of the dimensionless heat capacity. In particular, the smaller the heat capacity (i.e., the smaller the thermal inertia of the fluid upon a heat source), the higher the internal temperature as a consequence of the heat production caused by internal frictions. In such a case phase separation can be delayed in time or even completely prevented, so that miscibility appears to be extended by the shear even for temperatures which look to be macroscopically below the critical temperature, although actually such an extension of miscibility is due to the internal frictions, which raise the temperature locally above the critical temperature. The possibility to simulate such an interplay between hydrodynamics and thermodynamics is made possible by the use of the proposed thermodynamic-based diffuse interface model, which coherently integrates species, momentum, and energy balance.

D. The role of thermal conductivity

In all the previous simulations in this study, the physical properties of the mixture were considered independent of temperature and composition, that is, $\tilde{D} = \tilde{\eta} = \tilde{k} = \tilde{c} = 1$ in Eqs. (17a)–(17e). As a representative case of composition-dependent properties, let us assume here that the thermal conductivity of the mixture depends on mass fraction. In some previous works a linear dependence of $\tilde{k}$ from the mass fraction was assumed [32,44], while here a nonlinear dependence is considered, as follows:

$$\tilde{k} = b_1 \cdot {b_2}^{\phi/\phi_r}, \tag{28}$$

with $b_1 = 0.1$, $b_2 = 10$, and $\phi_r = \phi_0 = 0.4$ in the specific case under consideration. Such an expression is not intended to replicate the thermal conductivity of any real physical system; it only allows for capturing a strong nonlinear dependence of thermal conductivity. In particular, $\tilde{k}$ is unitary for the unseparated mixture at $t = 0$ when $\phi_0 = 0.4$ while, upon phase separation, the drops of the minority phase with $\phi > 0.5$ (i.e., the red ones) become significantly more conductive than the patches of the other phase (i.e., the blue one) by roughly a factor 40 for equilibrated phases at an average Margules coefficient of $(\Psi^+ + \Psi^-)/2 = 2.35$.

Figures 7 and 8 show two possible evolutions of the phase separation under a shear and a thermal gradient for such a composition-dependent thermal conductivity by considering $N_\alpha = 10^2$, $N_{\mathrm{Le}} = 10$, and $N_c^{-1} = 0$ as in Fig. 4. By using this parametric set, the capillary number is smaller than its critical value, thus resulting in the nucleation of stable droplets, and heat conduction is ten times faster than mass diffusion, at least for the initial unseparated mixture.

Figure 7 shows that phase separation starts from the upper cooler boundary by forming droplets moving rightward with flow ($\tilde{t} = 300$), further nucleating within the bulk of the domain as time progresses ($\tilde{t} = 600$) and then shifting their orientation as they move past the centerline of the

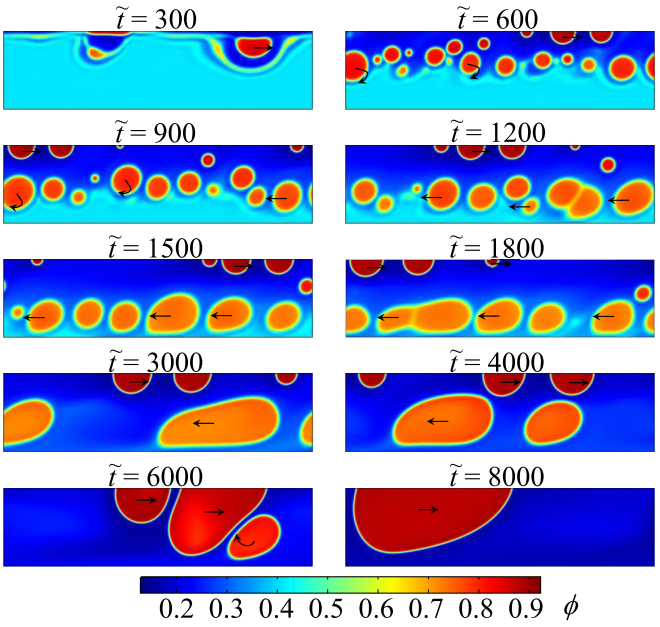

FIG. 7. Phase separation of a binary mixture having the composition-dependent thermal conductivity reported in Eq. (28), under a thermal gradient and for an imposed dimensionless shear rate of $\tilde{\gamma} = 10^{-2}$ with $N_{\mathrm{Le}} = 10$, $N_\alpha = 10^2$, and $N_c^{-1} = 0$. In this simulation round droplets nucleate at the top boundary.

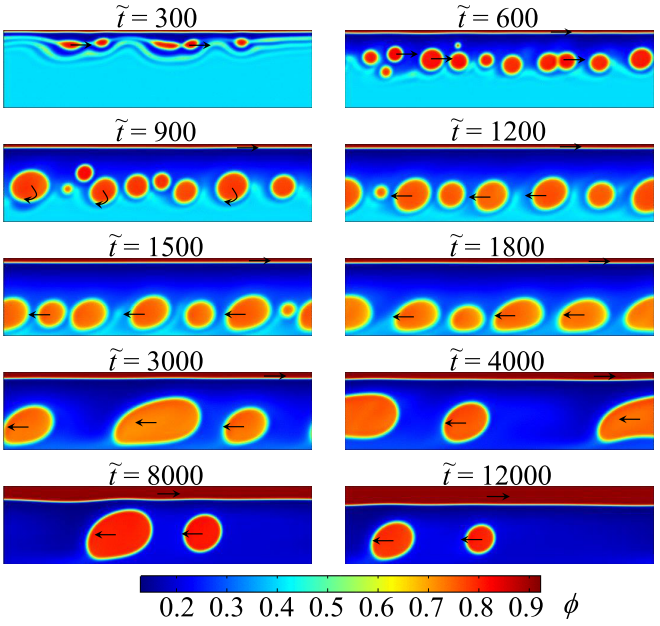

FIG. 8. Phase separation of a binary mixture having the composition-dependent thermal conductivity reported in Eq. (28), under a thermal gradient and for an imposed dimensionless shear rate of $\tilde{\gamma} = 10^{-2}$ with $N_{\mathrm{Le}} = 10$, $N_\alpha = 10^2$, and $N_c^{-1} = 0$. In this simulation an elongated stripe nucleates at the top boundary.

domain ($\tilde{t} = 900$). A careful comparison with the companion simulation in Fig. 4, which shares the same simulation parameters except for $\tilde{k} = 1$, shows that phase separation in Fig. 7 is comparatively slower than in Fig. 4. In particular, by comparing the snapshots at $\tilde{t} = 600$ and $\tilde{t} = 900$, we see that in Fig. 4 the droplets of the minority phase are characterized by a larger mass fraction (i.e., they are more red) and are closer to the bottom boundary than in Fig. 7. This is due to the thermal conductivity function [Eq. (28)], which makes the majority phase (i.e., in blue regions) less conductive, so that heat transport is hindered and the system cools down less rapidly than in Fig. 4. In turn, the Margules coefficient Ψ is smaller in Fig. 7, resulting in equilibrated phases with mass fractions closer to $\phi = 0.5$ (i.e., less red and less blue). Nevertheless, although the phase separation process proceeds slower, the core of the domain gets progressively cooler, so that droplets move downward ($\tilde{t} = 1200$) and move to the left by following the flow field ($\tilde{t} = 1500$). Over time, droplets coalesce ($\tilde{t} = 1800$), resulting in bigger droplets ($\tilde{t} = 3000$ and $\tilde{t} = 4000$), eventually merging with the droplets moving coherently with the top boundary ($\tilde{t} = 6000$) to produce a big droplet of the minority phase ($\tilde{t} = 8000$).

Figure 8 shows a different evolution of the system by using the same parameters but a different distribution of the random initial noise. Again phase separation starts from the top cooler boundary ($\tilde{t} = 300$); however, as clearer at $\tilde{t} = 600$, the initial nucleation produces a stripe of the minority phase at the top boundary, which moves rightward. Being it more thermally conductive than the unmixed blend, the system cools down and nucleation takes place even in the center of the domain ($\tilde{t} = 900$), with droplets following the flow field ($\tilde{t} = 1200$) and progressively coalescing with time ($\tilde{t} = 1800$ and $\tilde{t} = 3000$). In the meantime, the upper stripe becomes thicker at the expenses of the remaining droplets, which shrink according to mass diffusion ($\tilde{t} = 8000$ and $\tilde{t} = 12\,000$). Thus, although the final system configuration is characterized by a stripe (Fig. 8) instead of a large droplet (Fig. 7), the main features of the evolution dynamics remain the same of those described in Figs. 4 and 7, indicating that a composition-dependent thermal conductivity may affect the pace of phase separation, but it does not significantly change the characteristic fingerprint of spinodal decomposition under a thermal gradient, in fair agreement with previous investigations [44].

IV. CONCLUSIONS

In this work we present a thermodynamically consistent phase-field model which coherently comprises mass, species, momentum, and energy balance to simulate the phase separation of regular binary mixtures. Integrating the energy balance in the Cahn-Hilliard-Stokes-Korteweg equations requires a coherent description of the mixture thermodynamics, which provides a consistent framework to link together the Korteweg force, the surface tension, the driving force for spinodal decomposition, and the characteristic thickness of the diffuse interface, which otherwise would be erroneously treated as independent quantities. The proposed model was applied to the simulation of phase separation in a shear flow under a temperature gradient in order to showcase the complex interplay between fluid dynamics, heat transport, and mixture thermodynamics, which are summarized in a schematic diagram reported in Fig. 9.

Compared to previous investigations, numerical results evidenced that the dynamics of phase separation of a sheared mixture under a temperature gradient shows distinct characteristics compared to the instantaneous quench, whose behavior is approached when heat conduction is faster than mass diffusion, that is, for Lewis number (N_{Le}) larger than 10. However, in general, and especially for $N_{\mathrm{Le}} \leqslant 0.1$, the imposed temperature gradient causes a drift of emerging nuclei and droplets from low-temperature zones to high-temperature zones; when droplets cross the centerline, they change direction according to the different velocity field imposed by the shear flow. The capillary number (N_{Ca}) and the fluidity number (N_{α}) affect the dynamics of phase separation in the same way as in an instantaneous quench, leading to either droplet breakup and the formation of stripes when $N_{\mathrm{Ca}} > N_{\mathrm{Ca}}^{\mathrm{cr}}$ or stable, round droplets for $N_{\mathrm{Ca}} < N_{\mathrm{Ca}}^{\mathrm{cr}}$, with $N_{\mathrm{Ca}}^{\mathrm{cr}}$ denoting a critical capillary number. Nevertheless, compared to instantaneous quench, the symmetry of phase separation with respect to the domain centerline is broken, as the nucleation of stripes and droplets takes place preferentially

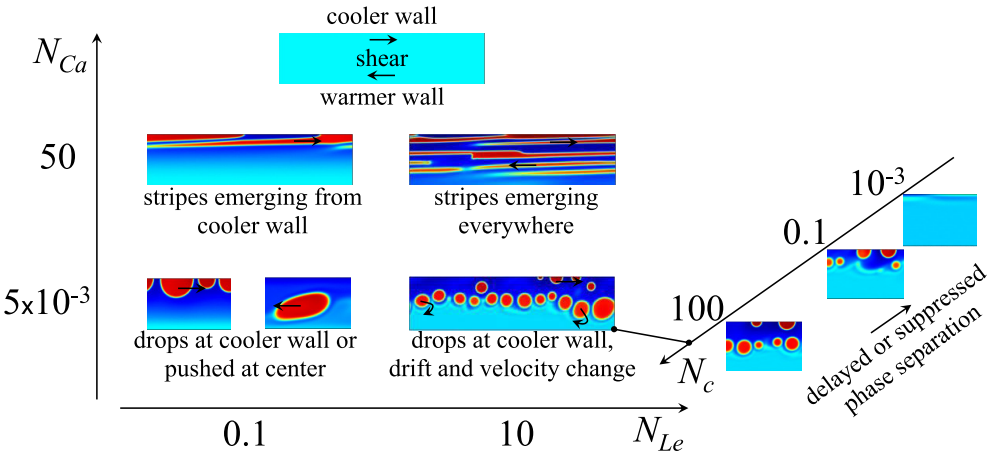

FIG. 9. Main results of the study summarized in a diagram which highlights the principal effects of capillary number, Lewis number, and dimensionless heat capacity on the regimes of nonisothermal phase separation of a sheared binary mixture.

at the cooler wall, where stable droplets may remain attached and move coherently with it. In the conditions of intermediate shear rate here simulated, fluid dynamics prevails and is only barely affected at the macroscale by phase separation and heat transport. As for the effect of the mixture thermal properties, simulations show that a decrease in the dimensionless heat capacity (N_c) causes a delay in the dynamics of phase separation, which can even be prevented for $N_c \leqslant 0.001$. Such an effect, which resembles a shear-induced extension of the mixture miscibility, is caused by the heat generated by the internal frictions, which raise the internal temperature above its critical value. A nonlinear dependence from the mass composition of the thermal conductivity showed that the pace of phase separation slows down when the conductivity of the majority phase is smaller than that of the minority phase; however, this effect does not change the characteristic behavior of spinodal decomposition under a temperature gradient.

The results here reported highlight that the phase-field model requires a thermodynamically consistent framework to coherently integrate mass, species, momentum, and energy balances, thus reducing the number of independent quantities without requiring any *ad hoc* assumptions. The implementation of the model in the finite-element software COMSOL MULTIPHYSICS makes it available to a wider audience, arguably extending the applicability, reproducibility, and accuracy compared to in-house codes. Future investigations will focus on the application of the numerical model to exploring the dynamics of phase separation in different hydrodynamic regimes and flow fields, in addition to applying model predictions for exploiting the diverse nucleation morphologies for innovative manufacturing routes of granular and soft materials.

ACKNOWLEDGMENT

This research received partial funding from the Headquarters of University Advancement at the National Cheng Kung University, which was sponsored by the Ministry of Education, Taiwan.

APPENDIX A: THERMODYNAMICS OF REGULAR BINARY MIXTURES

The state of a binary mixture at equilibrium is determined through a "coarse-grained" Gibbs free energy. Most mixtures, such as the acetone-hexadecane and benzene-cyclohexane mixtures that have been used by Mauri and co-workers in previous experimental work [58], are well described as regular mixtures, which means that their components and the mixtures themselves are both van der

Waals fluids (see the review by Levelt Sengers and Levelt [59]). As a consequence, it can be shown (see Chap. 7 of Sandler [60]) that regular mixtures have zero nonideal, or excess, volume and zero excess entropy [61], so that the only nonideality is in the excess enthalpy of mixing. In particular, for incompressible symmetric binary mixtures, as in our case, the excess enthalpy can be described in terms of a single, so-called Margules parameter, Ψ, so that the Gibbs free energy per unit mass g is

$$g(T,\phi) = g_0(T) + \Delta g^{id}(T,\phi) + g^E(T,\phi), \tag{A1}$$

which is independent of pressure as the mixture is regarded as incompressible.

Here, the first term on the RHS corresponds to the free energy of the two components before mixing, i.e., $g_0 = \phi g_1(T) + (1-\phi)g_2(T) = g_0(T)$, where we have considered that for symmetric mixtures $g_1 = g_2 = g_0$. The second term on the RHS of Eq. (A1) is the free energy of mixing of an ideal mixture, i.e., a mixture whose two components have identical properties, which, for species having the same molecular weight $M_1 = M_2 = M_w$, reads as

$$\Delta g^{id}(T,\phi) = R_w T[\phi \ln \phi + (1-\phi)\ln(1-\phi)], \tag{A2}$$

where $R_w = R/M_w$, with R denoting the ideal gas constant. Finally, the last term is the excess Gibbs free energy, accounting for the nonideality of the mixture. As mentioned above, assuming that the mixture is symmetric, g^E can be expressed as a function of a single Margules coefficient Ψ as

$$g^E = R_w T \Psi \phi(1-\phi), \tag{A3}$$

where $\Psi(T)$ is a function of the temperature T. We recall that the assumption of incompressibility (i.e., constant density) implies that pressure alone does not have any effect [47].

Consequently, the Gibbs free energy per unit mass is

$$g = g_0(T,\phi) + R_w T[\phi \ln \phi + (1-\phi)\ln(1-\phi)] + R_w T \Psi \phi(1-\phi). \tag{A4}$$

From the stability condition, which states that the mixture is stable as long as $\partial^2 g/\partial\phi^2 > 0$, we see that when $\Psi > 2$ the Gibbs free energy presents an instability region, i.e., a miscibility gap: when the overall composition of the mixture lies outside this region the mixture is stable, while when it lies inside this region the mixture separates into two coexisting phases [60]. On the contrary, when $\Psi < 2$, the mixture is stable at all compositions, so that $\Psi = 2$ defines a critical condition, at a critical temperature $T = T_c$. In addition, for regular binary mixtures, we must impose that the excess volume v^E and the excess entropy s^E are both equal to zero. The first condition, requiring that $v^E = \partial g^E/\partial p = 0$, is identically satisfied, considering that the mixture is incompressible. The latter condition, imposing that $s^E = -(\partial g^E/\partial T)_\phi = 0$, shows that $RT\Psi$ must be independent of T, that is $\Psi \propto T^{-1}$, and since $\Psi(T_c) = 2$ we find

$$\Psi = 2T_c/T. \tag{A5}$$

By using Eqs. (A3) and (A4) we also obtain the chemical potential difference μ_{12}:

$$\mu_{12} = \mu_1 - \mu_2 = \left(\frac{\partial g}{\partial \phi}\right)_T = R_w T \ln\frac{\phi}{1-\phi} + \mu_{12}^E; \quad \mu_{12}^E = R_w T \Psi(1-2\phi), \tag{A6}$$

and, by exploiting the thermodynamic equality $(\partial(g/R_wT)/\partial T)_\phi = -h/(R_w T^2)$, we obtain the partial enthalpy difference $\bar{h}_{12}$:

$$\bar{h}_{12} = -R_w T^2 \left(\frac{\partial(\mu_{12}/R_wT)}{\partial T}\right)_\phi = -R_w T^2 \frac{d\Psi}{dT}(1-2\phi) = R_w T \Psi(1-2\phi) = \bar{h}_{12}^E. \tag{A7}$$

Therefore, for regular symmetric mixtures, substituting Eq. (A5) these expressions become

$$\mu_{12}^E = 2R_w T_c(1-2\phi) = \bar{h}_{12}, \tag{A8}$$

and

$$\mu_{12} = R_w T \ln \frac{\phi}{1-\phi} + 2R_w T_c(1-2\phi). \tag{A9}$$

Finally, considering that for regular mixtures $u^E = h^E = g^E$ since $s^E = v^E = 0$, we find that the internal energy u is

$$u = u^{id} + u^E = c(T - T_{\text{ref}}) + R_w T \Psi \phi(1-\phi), \tag{A10}$$

where T_{ref} is a reference temperature and $c = c(T)$ is the specific heat of the ideal mixture, which does not depend on the composition [47].

APPENDIX B: THE GOVERNING EQUATIONS

The evolution of a multicomponent nonreactive mixture with n species subject to an external force field is described using the equations of conservation of mass, species, momentum, and energy reported in the following. For a comprehensive derivation of the conservation equations, the reader can refer to Chap. II in De Groot and Mazur [46] or to Tables 19.2-3 and 19.2-4 in Bird *et al.* [62].

$$\frac{D\rho}{Dt} + \rho \nabla \cdot \mathbf{v} = 0, \tag{B1}$$

$$\rho \frac{D\phi_i}{Dt} + \nabla \cdot \mathbf{J}_i = 0, \tag{B2}$$

$$\rho \frac{D\mathbf{v}}{Dt} + \nabla \cdot \mathbf{T} = \mathbf{F} = \rho \mathbf{f} = -\rho \sum_{i=1}^{n} \phi_i \nabla \psi_i \quad \text{with } \mathbf{T} = \mathbf{J}_v + p\mathbf{I} \quad \text{and } \mathbf{J}_v = \mathbf{J}'_v + p'\mathbf{I}, \tag{B3}$$

$$\rho \frac{Du}{Dt} + \nabla \cdot \mathbf{J}_u = \dot{q} = -\mathbf{T} : \nabla \mathbf{v} - \sum_{i=1}^{n} \mathbf{J}_i \cdot \nabla \psi_i, \tag{B4}$$

where $D/Dt = \partial/\partial t + \mathbf{v} \cdot \nabla$ indicates the material derivative, $\mathbf{v}$ is the mass average velocity, ϕ_i is the mass fraction of species i, u is the internal energy per unit mass, and ρ is the density. In addition, $\mathbf{f} = \sum_{i=1}^{n} \phi_i \mathbf{f}_i$, where $\mathbf{f}_i = -\nabla \psi_i$ is a conservative force per unit mass, with ψ_i denoting the potential of the force acting on the i th species. The last term in the RHS of Eq. (B4) represents the net energy entering a material volume due to conservative energy potentials. When the potential ψ_i is the same for all species (e.g., in the case of gravity, when $\psi_i = -gz$, with g being the gravity field acting along the direction z), such a net energy vanishes identically since the sum of all diffusive mass fluxes is zero. Conversely, when the potential ψ_i is different for each species (e.g., in the case of an electric field imposed to a mixture of species with different charges), the net energy entering the material volume can differ from zero (e.g., it represents the Joule dissipation heat in a charged system). In Eqs. (B3) and (B4) $\mathbf{T}$ is the stress tensor, $\mathbf{I}$ is the unitary identity tensor, while p and p' refer to the thermodynamic (i.e., hydrostatic) pressure and the nonthermodynamic pressure-like term (see Chap. 7.5 of Mauri [45]), defined so that $\mathbf{J}'_v$ is the deviatoric part of $\mathbf{T}$ (and of $\mathbf{J}_v$ as well). It is assumed that no body couples are applied to the system, so that the momentum flux tensor is considered symmetric. Finally, $\mathbf{J}_i$, $\mathbf{J}_u$, and $\mathbf{J}_v$ are the diffusive material, internal energy, and momentum fluxes, while $\dot{q}$ is the internal energy source, i.e., the increase of internal energy per unit time and per unit volume. For a detailed derivation of $\dot{q}$, the reader is referred to Chap. 7.4 and 7.5 of Mauri [45] or equivalently to Chap. II in De Groot and Mazur [46] [in particular Eq. (II-34)]. The same form of the energy equation appears also in Bird *et al.* [62] [Eq. (D) in Table 19.2-4, along with footnote *b*] and Slattery [63] (third equation in Table 8.5.2-1).

The diffusive fluxes are proportional to the thermodynamic forces through constitutive equations that can be determined applying nonequilibrium thermodynamics. To do that, consider the entropy

conservation equation [see Eq. (III-25) in De Groot and Mazur [46] or Eq. (7.64) in Mauri [45]]:

$$\rho \frac{Ds}{Dt} + \nabla \cdot \mathbf{J}_s = \sigma_s, \tag{B5}$$

where s is the mixture entropy per unit mass, $\mathbf{J}_s$ is the diffusive entropy flux, while σ_s is the entropy production term (see Eq. (7.70) in Mauri [45]):

$$\sigma_s = -\frac{1}{T^2}\mathbf{J'}_u \cdot \nabla T - \frac{1}{T}\sum_{i=1}^{n} \mathbf{J}_i.([\nabla \mu_i]_T + \nabla \psi_i) - \frac{1}{T}(\mathbf{T} - p\mathbf{I}) : \nabla \mathbf{v}. \tag{B6}$$

Here, T is the temperature, $[\nabla \mu]_T$ indicates the gradient of any quantity $\mu(T, \phi)$, taken at constant T (note that the thermodynamic properties of the incompressible mixture are independent of the pressure), $\mathbf{J'}_u = \mathbf{J}_u - \sum_{i=1}^{n} \mathbf{J}_i \bar{h}_i$ is an energy flux (see Eq. (7.69) in Mauri [45]), where $\bar{h}_i$ is the partial enthalpy of species i, μ_i is the chemical potential per unit mass (i.e., the partial Gibbs energy) of species i, and $\mathbf{T} - p\mathbf{I} = \mathbf{J}_v = \mathbf{J'}_v + p'\mathbf{I}$ [see Eq. (B3)]. Now, applying the rules of nonequilibrium thermodynamics, i.e., assuming linear relations between forces and fluxes, and considering that the system is isotropic (i.e., applying the Curie symmetry principle), neglecting all coupling terms (i.e., no Soret and Dufour effects), and imposing that the sum of the diffusive species fluxes is nil (i.e., $\mathbf{J}_n = -\sum_{i=1}^{n-1} \mathbf{J}_i$), we obtain the following constitutive equations (see Chap. 8 in Mauri [45]):

$$p' = -\zeta \nabla \cdot \mathbf{v}, \tag{B7}$$

$$\mathbf{J}_i = -\sum_{j=1}^{n-1} \frac{M_j \rho}{RT} D_{ij}([\nabla \mu_{jn}]_T + \nabla \psi_{jn}), \tag{B8}$$

$$\mathbf{J'}_u = \mathbf{J}_u - \sum_{i=1}^{n-1} \mathbf{J}_i \bar{h}_{in} = -k \nabla T, \tag{B9}$$

$$\mathbf{J'}_v = -\eta \left(\nabla \mathbf{v} + \nabla \mathbf{v}^{\mathrm{T}} - \frac{2}{3}(\nabla \cdot \mathbf{v})\mathbf{I} \right), \tag{B10}$$

where ζ is the bulk viscosity, D_{ij} are the diffusion coefficients, k is the thermal conductivity, and η is the viscosity, with $\mu_{jn} = \mu_j - \mu_n$, $\psi_{jn} = \psi_j - \psi_n$, and $\bar{h}_{jn} = \bar{h}_j - \bar{h}_n$ denoting the differences of chemical potential, conservative energy potential, and partial enthalpy between species j and n. In Eq. (B10), it is worth noting that $\mathbf{J'}_v$ is directly proportional to the deviatoric symmetric part of the velocity gradient tensor. Note also that the use of constitutive equations (B7)–(B10) makes the entropy production term σ_s in Eq. (B6) strictly positive, so that the system evolution satisfies the second law of thermodynamics.

In our case, we are considering binary mixtures, with $\phi_1 = \phi$, $\mathbf{J}_1 = \mathbf{J}_\phi$, and $\phi_2 = 1 - \phi$, $\mathbf{J}_2 = -\mathbf{J}_\phi$. In addition, our model relies on the following simplifying assumptions: (i) the two species in the mixture have the same molecular weight $M_1 = M_2 = M_w$, so that molar and mass fractions coincide, and (ii) ρ is constant (i.e., the mixture is incompressible). Therefore, the governing equations become

$$\frac{D\rho}{Dt} + \rho \nabla \cdot \mathbf{v} = 0, \tag{B11}$$

$$\rho \frac{D\phi}{Dt} + \nabla \cdot \mathbf{J}_\phi = 0 \quad \text{with } \mathbf{J}_\phi = -\frac{\rho D_{12}}{R_w T}([\nabla \mu_{12}]_T + \nabla \psi_{12}), \tag{B12}$$

$$\rho \frac{D\mathbf{v}}{Dt} + \nabla \cdot \mathbf{J}_v = -\nabla p - \rho \phi \nabla \psi_{12} \quad \text{with } \mathbf{J}_v = -\eta(\nabla \mathbf{v} + \nabla \mathbf{v}^{\mathrm{T}}), \tag{B13}$$

$$\rho \frac{Du}{Dt} + \nabla \cdot \mathbf{J}_u = -\mathbf{J}_v : \nabla \mathbf{v} - \mathbf{J}_\phi \cdot \nabla \psi_{12} \quad \text{with } \mathbf{J}_u = -k \nabla T + \bar{h}_{12} \mathbf{J}_\phi, \tag{B14}$$

where we have denoted $\mu_{12} = \mu_1 - \mu_2$ and $\psi_{12} = \psi_1 - \psi_2$. It should be stressed that for a mixture with constant density Eq. (B11) gives $\nabla \cdot \mathbf{v} = 0$, thus $p' = 0$ [see Eq. (B7)], $\mathbf{J}_v = \mathbf{J}'_v$ [see Eq. (B3)], with $\mathbf{J}_v$ that reduces to Eq. (B13) [compare it with Eq. (B10)], and so $\mathbf{T} : \nabla\mathbf{v} = \mathbf{J}_v : \nabla\mathbf{v}$ [compare Eq. (B4) with Eq. (B14)]. Finally, as shown in our previous study [43], the term $-\rho\nabla\psi_2$ on the RHS of Eq. (B3) can be adsorbed into the pressure p in Eq. (B13).

Equations (B12) and (B14) must be coupled with Eqs. (A7), (A9), and (A10), indicating partial enthalpies, chemical potentials, and internal energy as functions of T and ϕ. The expression of the potential difference ψ_{12} of the conservative body force entering Eqs. (B12)–(B14) is reported in Appendix C. Mixture properties such as thermal conductivity, k, viscosity, η, and the diffusivity, D_{12}, are known functions of T and ϕ. While the thermal conductivity and the viscosity can even be regarded as constant as a first approximation, a dependence of the diffusion coefficient D_{12} on the composition should be considered. In fact, in ideal mixtures (i.e., when $\Psi = 0$, which also implies $\psi_{12} = 0$ as shown in Appendix C), substituting Eq. (A6) into the constitutive equation for the diffusive mass flux [Eq. (B12)] results in

$$\mathbf{J}_\phi = -\frac{\rho D_{12}}{R_w T}[\nabla\mu_{12}]_T = -D_{12}[\phi(1-\phi)]^{-1}\nabla\phi, \tag{B15}$$

predicting diverging fluxes in the dilute limit. Therefore, imposing that as $\phi \to 0$(or $\phi \to 1$) Fick's law must be recovered, i.e., $\mathbf{J}_\phi = -\rho D\nabla\phi$, the following expression for the diffusion coefficient is considered [47,64]:

$$D_{12}(\phi, T) = D(T)\phi(1-\phi), \tag{B16}$$

where D is a concentration-independent diffusion coefficient.

APPENDIX C: THE NONLOCAL KORTEWEG FORCES

In both Sec. II and Appendix B we referred to ψ_{12} as the difference between the potentials of all conservative force fields applied to the two components of the incompressible binary mixture. A particularly important example is the Korteweg force, which is a nonequilibrium and reversible body force which captures the capillary stresses at the interfaces of a two-phase system [18,43]. The Korteweg force can be derived by extending the free-energy functional, $\widehat{g}$, in order to account also for the gradients of the mass fraction, ϕ, arising from spatial inhomogeneities, that is [20]

$$\widehat{g}(\phi, \nabla\phi, T) = g(\phi, T) + g^{nl}(\nabla\phi, T), \tag{C1}$$

where $\widehat{g}$ is the generalized free energy per unit mass, g is the thermodynamic free energy [Eq. (A4)], which refers to the local bulk-state variables, while g^{nl} is its, so-called, nonlocal component, indicating the extra energy stored within the interfacial region [26]. Expressing g^{nl} in terms of a power series of $\nabla\phi$, assuming that the mixture is locally isotropic and with $M_1 = M_2 = M_w$, we find at leading order [20,26]

$$g^{nl} = \tfrac{1}{2}R_w T a^2(\nabla\phi)^2, \tag{C2}$$

where a is a characteristic length. It must be clear that this nonlocal term is relevant only in regions where $\nabla\phi$ is very large, that is when the mixture is separated in two phases, so that there is an interphase region, where the mass fraction ϕ changes rapidly.

Macroscopically, the two coexisting phases are separated by a sharp interfacial surface which, at equilibrium, is characterized by a surface tension, expressing the energy stored per unit interfacial area. Therefore, imposing that at equilibrium the line integral of the Gibbs free energy across the interfacial region at equilibrium equals the surface tension [49], the characteristic length a appears to be proportional to the surface tension σ, i.e.,

$$a = \sigma/(\kappa\rho R_w T), \tag{C3}$$

where κ is the dimensionless magnitude of the line integral [see Eq. (10)].

Using the generalized free energy, $\widehat{G} = \widehat{g} \cdot \sum_{i=1}^{2} m_i$, where m_i is the species mass, the generalized chemical potential of the species $\widehat{\mu}_i$ in the binary mixture can be obtained as

$$\widehat{\mu}_i = \left(\frac{\delta \widehat{G}}{\delta m_i}\right)_{T,p,m_{j\neq i}} = \widehat{g} + (1-\phi_i)\frac{\delta \widehat{g}}{\delta \phi_i}, \tag{C4}$$

where the variational derivative is [65]

$$\frac{\delta \widehat{g}}{\delta \phi_i} = \frac{\partial \widehat{g}}{\partial \phi_i} - \nabla \cdot \frac{\partial \widehat{g}}{\partial (\nabla \phi_i)}. \tag{C5}$$

Hence, decoupling the generalized chemical potential $\widehat{\mu}_i$ into the thermodynamic potential μ_i and the nonlocal potential ψ_i, that is, $\widehat{\mu}_i = \mu_i + \psi_i$, we get that the latter is

$$\psi_i = g^{nl} + (1-\phi_i)\frac{\partial g^{nl}}{\partial \phi_i} - (1-\phi_i)\,\nabla \cdot \frac{\partial g^{nl}}{\partial \nabla \phi_i} = g^{nl} + (1-\phi_i)\frac{\partial g^{nl}}{\partial \phi_i} - (1-\phi_i)\,R_w T a^2 \nabla^2 \phi_i. \tag{C6}$$

Thus, by expressing the potential energy differences, we get

$$\widehat{\mu}_{12} = \frac{\delta \widehat{g}}{\delta \phi} = \frac{\partial \widehat{g}}{\partial \phi} - \nabla \cdot \frac{\partial g^{nl}}{\partial \nabla \phi} = \mu_{12} + \psi_{12} \quad \text{and} \quad \psi_{12} = -R_w T a^2 \nabla^2 \phi, \tag{C7}$$

where μ_{12} is the thermodynamic chemical potential difference, Eq. (A9), while ψ_{12} is its nonlocal counterpart, which is used in Eqs. (B12)–(B14) and reported in Eq. (8).

The so-called Korteweg force, i.e., a reversible generalized body force (per unit volume) is then given by

$$\mathbf{F} = -\rho \sum_{i=1}^{2} \phi_i \nabla \psi_i = \underbrace{-\rho \phi \nabla \psi_{12}}_{\mathbf{F}_\phi} - \underbrace{\rho \nabla \psi_2}_{\text{absorbed in } p}; \quad \mathbf{F}_\phi = \rho R_w \phi \nabla (a^2 T \nabla^2 \phi), \tag{C8}$$

where we denoted the gradient of a scalar that can be adsorbed in the pressure term [43] and the resulting force $\mathbf{F}_\phi$, used in Eqs. (3) and (7). Equation (C8) is in the form obtained by Lamorgese *et al.* [26] by generalizing a variational scheme by Serrin [66]; the same result, where however the reversibility of the resulting force is assumed *a priori*, can be obtained by applying Noether's theorem, as shown by Anderson *et al.* [49], or by the least action principle, as shown by Lowengrub and Truskinovsky [67].

As shown by Van Laar, regular mixtures are composed of two van der Waals fluids and also behave themselves as van der Waals fluids. In that case, it was shown [18] that in Eq. (C7) ψ_{12} does not depend on T, so that Ta^2 is a constant that we can set equal to $T_c \hat{a}^2$, where $\hat{a}$ is a constant characteristic length; therefore, we get

$$\psi_{12} = -R_w T_c \hat{a}^2 \nabla^2 \phi \quad \text{and} \quad a = \hat{a}\sqrt{T_c/T}. \tag{C9}$$

We assume that this relation is satisfied in all binary mixtures of interest.

[1] P. Debenedetti, *Metastable Liquids: Concepts and Principles* (Princeton University Press, Princeton, 1996).
[2] E. M. Lifshitz and L. P. Pitaevskii, *Physical Kinetics* (Pergamon Press, New York, 1984).
[3] E. D. Siggia, Late stages of spinodal decomposition in binary mixtures, Phys. Rev. A **20**, 595 (1979).
[4] Y. C. Chou and W. I. Goldburg, Angular distribution of light scattered from critically quenched liquid mixtures, Phys. Rev. A **23**, 858 (1981).

[5] N.-C. Wong and C. M. Knobler, Light-scattering studies of phase separation in isobutyric acid + water mixtures: Hydrodynamic effects, Phys. Rev. A **24**, 3205 (1981).
[6] I. M. Lifshitz and V. V. Slyozov, The kinetics of precipitation from supersaturated solid solutions, J. Phys. Chem. Solids **19**, 35 (1961).
[7] W. R. White and P. Wiltzius, Real Space Measurement of Structure in Phase Separating Binary Fluid Mixtures, Phys. Rev. Lett. **75**, 3012 (1995).
[8] H. Furukawa, Dynamics of phase separation of a simple fluid mixture: Comparison between molecular dynamics and numerical integration of the phenomenological equation, Phys. Rev. E **55**, 1150 (1997).
[9] J. D. Gunton, M. San Miguel, and P. S. Sahni, in *Phase Transitions and Critical Phenomena*, edited by C. Domb and J. L. Lebowitz (Academic Press, New York, 1983), Vol. 8.
[10] P. Guenoun, R. Gastaud, F. Perrot, and D. Beysens, Spinodal decomposition patterns in an isodensity critical binary fluid: Direct-visualization and light-scattering analyses, Phys. Rev. A **36**, 4876 (1987).
[11] R. Gupta, R. Mauri, and R. Shinnar, Phase separation of liquid mixtures in the presence of surfactants, Ind. Eng. Chem. Res. **38**, 2418 (1999).
[12] P. Poesio, G. Cominardi, A. M. Lezzi, R. Mauri, and G. P. Beretta, Effects of quenching rate and viscosity on spinodal decomposition, Phys. Rev. E **74**, 011507 (2006).
[13] H. A. Stone, Dynamics of drop deformation and breakup in viscous fluids, Annu. Rev. Fluid Mech. **26**, 65 (1994).
[14] J. van der Waals, The thermodynamic theory of capillarity under the hypothesis of a continuous variation of density (Reprinted), J. Stat. Phys. **20**, 200 (1979).
[15] D. Jacqmin, Contact-line dynamics of a diffuse fluid interface, J. Fluid Mech. **402**, 57 (2000).
[16] L. M. Pismen, Nonlocal diffuse interface theory of thin films and the moving contact line, Phys. Rev. E **64**, 021603 (2001).
[17] D. N. Sibley, A. Nold, and S. Kalliadasis, Unifying binary fluid diffuse-interface models in the sharp-interface limit, J. Fluid Mech. **736**, 5 (2013).
[18] A. Lamorgese, R. Mauri, and L. M. C. Sagis, Modeling soft interface dominated systems: A comparison of phase field and Gibbs dividing surface models, Phys. Rep. **675**, 1 (2017).
[19] L. D. Landau and E. M. Lifshitz, *Statistical Physics*, Part 2, 3rd ed. (Pergamon Press, Oxford, 1980), pp. 85–140.
[20] J. W. Cahn and J. E. Hilliard, Free energy of a nonuniform system. I. Interfacial free energy, J. Chem. Phys. **28**, 258 (1958).
[21] J. W. Cahn and J. E. Hilliard, Free energy of a nonuniform system. III. Nucleation in a two-component incompressible fluid, J. Chem. Phys. **31**, 688 (1959).
[22] N. Vladimirova, A. Malagoli, and R. Mauri, Diffusion-driven phase separation of deeply quenched mixtures, Phys. Rev. E **58**, 7691 (1998).
[23] D. J. Korteweg, Sur la forme que prennent les équations du mouvement des fluides si l'on tient compte des forces capillaires causées par des variations de densité considérables mais continues et sur la théorie de la capillarité dans l'hypothèse d'une variation continue de la densité, Arch. Néerlandaises Sci. Exactes Nat. **6**, 1 (1901).
[24] P. C. Hohenberg and B. I. Halperin, Theory of dynamic critical phenomena, Rev. Mod. Phys. **49**, 435 (1977).
[25] N. Vladimirova, A. Malagoli, and R. Mauri, Two-dimensional model of phase segregation in liquid binary mixtures, Phys. Rev. E **60**, 6968 (1999).
[26] A. G. Lamorgese, D. Molin, and R. Mauri, Phase field approach to multiphase flow modeling, Milan J. Math. **79**, 597 (2011).
[27] A. E. Komrakova, O. Shardt, D. Eskin, and J. J. Derksen, Lattice Boltzmann simulations of drop deformation and breakup in shear flow, Int. J. Multiphase Flow **59**, 24 (2014).
[28] T. Kékesi, G. Amberg, and L. Prahl Wittberg, Drop deformation and breakup in flows with shear, Chem. Eng. Sci. **140**, 319 (2016).
[29] A. E. Komrakova, O. Shardt, D. Eskin, and J. J. Derksen, Effects of dispersed phase viscosity on drop deformation and breakup in inertial shear flow, Chem. Eng. Sci. **126**, 150 (2015).

[30] O. Shardt, S. K. Mitra, and J. J. Derksen, The critical conditions for coalescence in phase field simulations of colliding droplets in shear, Langmuir **30**, 14416 (2014).
[31] H. Wang, X. Li, K. Lin, and X. Geng, Morphological simulation of phase separation coupled oscillation shear and varying temperature fields, J. Low Temp. Phys. **191**, 153 (2018).
[32] D. Molin and R. Mauri, Spinodal decomposition of binary mixtures with composition-dependent heat conductivities, Chem. Eng. Sci. **63**, 2402 (2008).
[33] D. Bedeaux, E. Johannessen, and A. Røsjorde, The nonequilibrium van der Waals square gradient model. (I). The model and its numerical solution, Physica A **330**, 329 (2003).
[34] A. Onuki, Dynamic van der Waals theory, Phys. Rev. E **75**, 036304 (2007).
[35] O. Penrose and P. C. Fife, Thermodynamically consistent models of phase-field type for the kinetic of phase transitions, Phys. D: Nonlinear Phenom. **43**, 44 (1990).
[36] O. Penrose and P. C. Fife, On the relation between the standard phase-field model and a "thermodynamically consistent" phase-field model, Phys. D: Nonlinear Phenom. **69**, 107 (1993).
[37] H. W. Alt and I. Pawlow, A mathematical model of dynamics of non-isothermal phase separation, Phys. D: Nonlinear Phenom. **59**, 389 (1992).
[38] S.-L. Wang, R. F. Sekerka, A. A. Wheeler, B. T. Murray, S. R. Coriell, R. J. Braun, and G. B. McFadden, Thermodynamically-consistent phase-field models for solidification, Phys. D: Nonlinear Phenom. **69**, 189 (1993).
[39] M. Fabrizio, C. Giorgi, and A. Morro, A thermodynamic approach to non-isothermal phase-field evolution in continuum physics, Phys. D **214**, 144 (2006).
[40] D. Molin and R. Mauri, Enhanced heat transport during phase separation of liquid binary mixtures, Phys. Fluids **19**, 074102 (2007).
[41] P. Poesio, A. M. Lezzi, and G. P. Beretta, Evidence of convective heat transfer enhancement induced by spinodal decomposition, Phys. Rev. E **75**, 066306 (2007).
[42] V. Segal, Enhancement of Heat Transfer Rates Through Binary Mixtures Phase Separation, Ph.D. thesis, Tel Aviv University (2018).
[43] C.-C. Chueh, A. Bertei, and R. Mauri, Dynamics of phase separation of sheared inertialess binary mixtures, Phys. Fluids **32**, 023307 (2020).
[44] A. Bertei, B. Tellini, and R. Mauri, Dynamic transition of dendrite orientation in the diffusive spinodal decomposition of binary mixtures under a thermal gradient, Chem. Eng. Sci. **203**, 450 (2019).
[45] R. Mauri, *Non-equilibrium Thermodynamics in Multiphase Flows* (Springer, Dordrecht, 2013).
[46] S. R. de Groot and P. Mazur, *Non-equilibrium Thermodynamics* (Dover, New York, 1962).
[47] A. Bertei, A. Lamorgese, and R. Mauri, Constitutive relations of thermal and mass diffusion, J. Non-Equilibrium Thermodyn. **45**, 27 (2020).
[48] R. Mauri and A. Bertei, Non-local phase field revisited, J. Stat. Mech. (2021) 063212.
[49] D. M. Anderson, G. B. McFadden, and A. A. Wheeler, Diffuse-interface methods in fluid mechanics, Annu. Rev. Fluid Mech. **30**, 139 (1998).
[50] A. G. Lamorgese and R. Mauri, Phase-field modeling of interfacial dynamics in emulsion flows: Nonequilibrium surface tension, Int. J. Multiph. Flow **85**, 164 (2016).
[51] H. Tanaka and T. Araki, Spontaneous Double Phase Separation Induced by Rapid Hydrodynamic Coarsening in Two-Dimensional Fluid Mixtures, Phys. Rev. Lett. **81**, 389 (1998).
[52] A. G. Lamorgese and R. Mauri, Mixing of macroscopically quiescent liquid mixtures, Phys. Fluids **18**, 044107 (2006).
[53] N. Vladimirova, A. Malagoli, and R. Mauri, Two-dimensional model of phase segregation in liquid binary mixtures with an initial concentration gradient, Chem. Eng. Sci. **55**, 6109 (2000).
[54] F. Llovell, N. Mac Dowell, F. J. Blas, A. Galindo, and G. Jackson, Application of the SAFT-VR density functional theory to the prediction of the interfacial properties of mixtures of relevance to reservoir engineering, Fluid Phase Equilib. **336**, 137 (2012).
[55] Comsol Inc., Comsol Multiphysics user's guide, version 5.5, Burlington, MA (2019).
[56] V. Cristini, S. Guido, A. Alfani, J. Bławzdziewicz, and M. Loewenberg, Drop breakup and fragment size distribution in shear flow, J. Rheol. **47**, 1283 (2003).
[57] L. G. Leal, Flow induced coalescence of drops in a viscous fluid, Phys. Fluids **16**, 1833 (2004).

[58] F. Califano and R. Mauri, Retardation of the phase segregation of liquid mixtures with a critical point of miscibility, AIChE J. **64**, 4047 (2018).
[59] J. Levelt Sengers and A. H. M. Levelt, Diederik Korteweg, pioneer of criticality, Phys. Today **55**(12), 47 (2002).
[60] S. I. Sandler, *Chemical, Biochemical and Engineering Thermodynamics*, 4th ed. (Wiley, New York, 2006).
[61] J. H. Hildebrand, The term "regular solution," Nature (London) **168**, 868 (1951).
[62] R. B. Bird, W. E. Stewart, and E. N. Lightfoot, *Transport Phenomena*, 2nd ed. (John Wiley & Sons, New York, 2002), pp. 588–589.
[63] J. C. Slattery, *Advanced Transport Phenomena* (Cambridge University Press, Cambridge, 1999), p. 480.
[64] R. Mauri, R. Shinnar, and G. Triantafyllou, Spinodal decomposition in binary mixtures, Phys. Rev. E **53**, 2613 (1996).
[65] I. M. Gelfand and S. V. Fomin, *Calculus of Variations* (Prentice-Hall, Englewood Cliffs, NJ, 1963).
[66] J. Serrin, in *Encyclopedia of Physics*, edited by S. Flügge and C. A. Truesdell (Springer-Verlag, Berlin, 1959), Vol. VIII/1, p. 125.
[67] J. Lowengrub and L. Truskinovsky, Quasi–incompressible Cahn–Hilliard fluids and topological transitions, Proc. R. Soc. London A **454**, 2617 (1998).